Chapter 4

Analysis overview

This chapter aims to give an introduction to the search for electroweakinos presented in this work. First, the targeted final state is introduced and motivated, followed by the Standard Model of Particle Physics (SM) background processes that need to be considered when performing searches for Supersymmetry (SUSY) in this final state. Next, the reconstruction and identification of physics objects as well as the event selection requirements are described.

4.1 Search for electroweakinos in the 1-lepton final state

In the search for electroweakinos presented herein, the simplified model introduced in section 1.3.2 is interpreted in a final state with one lepton, two b-jets and high missing transverse momentum. This final state can occur when the W boson decays through $W^\pm \to \ell^\pm \nu_\ell$, while the Higgs boson decays into $h \to b\bar{b}$. Although a final state without leptons would benefit from the higher branching fraction of the $W^\pm \to q'\bar{q}$ decay, due to the large quantum chromodynamics (QCD) couplings these final states are largely dominated by QCD multi-jet background processes that are omnipresent at hadron colliders like the Large Hadron Collider (LHC). Final states with exactly one lepton have lower cross sections but allow to reject a majority of the QCD background, as pure QCD multi-jet events can only enter the 1-lepton final state through false reconstruction of a jet as a lepton (so-called *fake* leptons).

Targeting the decay of the Higgs boson into a pair of b quarks benefits from the high branching ratio of 58.3% of this decay mode and allows a full reconstruction of Higgs candidates, a procedure that will be used in the following to achieve a high signal-to-background ratio. Figure 4.1 shows the full signal model targeted in this search, including the considered decays of the W and Higgs bosons.

Previous searches for electroweakinos in this final state have been performed by the ATLAS [167, 168] and CMS [169] collaborations, and have excluded $\tilde{\chi}_1^\pm/\tilde{\chi}_2^0$ masses up to 540 GeV and 490 GeV, respectively, for massless $\tilde{\chi}_1^0$. The two previous ATLAS searches used 20.3 fb^{-1} of $\sqrt{s} = 8$ TeV and 36.1 fb^{-1} of $\sqrt{s} = 13$ TeV pp collision data, respectively. As opposed to this, the search presented in the following uses the full dataset available from the Run 2 data taking period, amounting to an unprecedented 139 fb^{-1} of pp collision data at $\sqrt{s} = 13$ TeV [170]. As
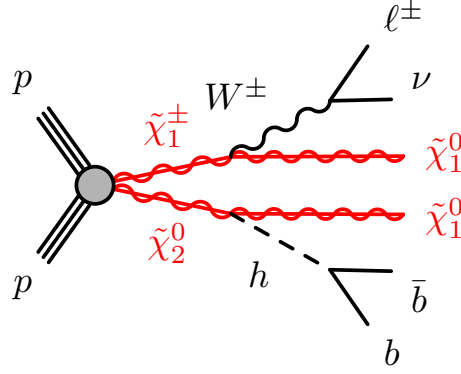
Figure 4.1: Diagram for the simplified model used in this work including the decays $W^{\pm} \to \ell^{\pm}\nu_{\ell}$ and $h \to b\bar{b}$.

this search analysis events in final states with exactly one lepton, it will often be referred to as the *1-lepton analysis* in the following.

4.2   Standard Model backgrounds

Although the requirement of exactly one lepton isolated from surrounding hadronic activity significantly reduces the contribution from QCD multi-jet background, numerous other SM processes can result in final states with exactly one isolated lepton, multiple jets and missing transverse momentum. Background sources are generally classified into *reducible* and *irreducible* backgrounds. Irreducible backgrounds are processes that have a physical phase space that is indistinguishable from the final state of the signal process considered. Reducible backgrounds, on the other hand, result from partially misreconstructed processes as well as mismeasurements. Examples of reducible processes are events where a lepton originates from a heavy flavour (HF) decay, photon conversions or misreconstructed jets. SM processes that result in final states with an isolated lepton, multiple jets and missing transverse momentum typically involve a W boson decaying into a lepton–neutrino pair (a so-called *leptonic decay*). The neutrino will contribute to the total missing transverse momentum in the event, while additional jets can appear in the final state through QCD radiation or other branches of the decay chain.

By far the largest SM background contribution stems from the production of top quarks, predominantly through top quark pair $t\bar{t}$ production, where both top quarks decay into a W boson and a b quark. Final states with one isolated lepton can occur through leptonic decay of one of the W bosons. Figure 4.2(a) shows a diagram of an exemplary decay of a $t\bar{t}$ system into a final state with one lepton, multiple jets (two of which originate from b quarks) and missing transverse momentum. In addition to $t\bar{t}$, single top production (*s*-channel, *t*-channel or tW-channel) can also result in similar final states as the SUSY signal and thus constitutes a significant SM background process. An exemplary decay into a final state relevant for this search is shown in fig. 4.2(b).

Apart from processes involving top quarks, the production of a W boson in association with multiple jets ($W + $ jets) is the third major background considered in the analysis. If the W boson undergoes a leptonic decay and two of the produced jets are tagged as originating from
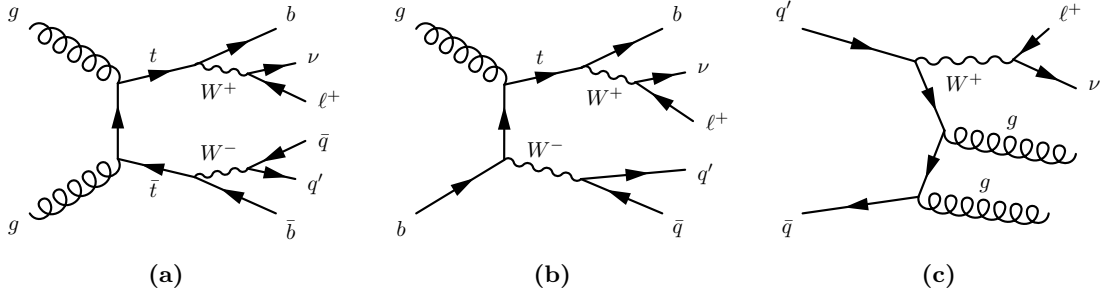
Figure 4.2: Exemplary Feynman diagrams showing the dominant processes (a) $t\bar{t}$, (b) single top and (c) W + jets production with subsequent decays.

b quarks, the signature of this process can be similar to that of signal events. An exemplary diagram for a W + jets event is shown in fig. 4.2(c).

Production of multiple vector bosons V $(= W, Z)$—although not a dominant background due to low cross sections—can still result in the same final state as the signal process. In the following, diboson VV and multiboson VVV processes are considered.

Other SM backgrounds with small contributions in the phases spaces targeted by the analysis include Z + jets production, $t\bar{t} + V$ production, as well as various processes involving Higgs bosons. Z + jets plays only a minor role, as the only irreducible component is $Z(\rightarrow \tau\tau)$ + jets, where one τ-lepton undergoes a leptonic decay and the other one a hadronic decay. Production of $t\bar{t} + V$ has a similar topology as ordinary $t\bar{t}$ processes but with lower cross section and additional objects in the final state. Higgs processes considered in the following include single Higgs production through vector boson fusion (VBF) or gluon–gluon fusion (ggF) as well as $h + V$ and $h + t\bar{t}$ processes. In the following, these backgrounds are grouped together and labelled as *other* backgrounds.

Pure QCD multi-jet events can only appear in the 1-lepton final state through false reconstruction of a jet as a lepton (so-called *fake* leptons) and mismeasurement of $E_{\mathrm{T}}^{\mathrm{miss}}$. It has been shown that this background is negligible in all selections relevant to this search, hence no estimation for QCD contribution is considered in the following [170].

4.3   Monte Carlo samples

Table 4.1 summarises all Monte Carlo (MC) generators and software versions run during generation of the simulated events used in the following. Further details are given in the relevant ATLAS simulation notes [171–174].

4.3.1   Signal samples

The $\tilde{\chi}_1^\pm/\tilde{\chi}_2^0$ pair production signal samples were generated at leading order (LO) using MAD-GRAPH5_AMC@NLO 2.6.2 [175, 176] with up to two additional partons in the matrix element (ME). MADGRAPH5_AMC@NLO is interfaced with PYTHIA8 [177] for the parton shower (PS), hadronisation and underlying event, using the CKKW-L [178] scheme for matching the

PS to the MEs. The NNPDF 2.3 LO [179] parton distribution function (PDF) set and the A14 set of tuned parameters [180] are used. For modelling the decay of HF quarks, EvtGen v1.6 [181] is used.

As the $\tilde{\chi}_1^\pm/\tilde{\chi}_2^0$ and $\tilde{\chi}_1^0$ masses are free parameters of the signal model, they are systematically scanned, resulting in a set of 164 distinct signal models evenly distributed in the two-dimensional grid spanned by the two mass parameters. In the following, this two-dimensional grid will be referred to as *signal grid*, while the distinct signal scenarios (each with a unique set of mass parameter values) will be referred to as *signal points*. The generated signal grid covers $\tilde{\chi}_1^\pm/\tilde{\chi}_2^0$ masses from 150 GeV to 1.1 TeV and $\tilde{\chi}_1^0$ masses from 0 GeV to 550 GeV, avoiding the kinematically forbidden region with $m(\tilde{\chi}_1^\pm/\tilde{\chi}_2^0) < m(\tilde{\chi}_1^0) + m(h)$ that does not allow for production of on-shell Higgs bosons.

Signal samples well within the expected sensitivity range of the analysis, i.e. with relatively low $\tilde{\chi}_1^\pm/\tilde{\chi}_2^0$ and $\tilde{\chi}_1^0$ masses or already excluded at 95% CL by previous analyses, are generated using the ATLFAST-II detector simulation. The full detector simulation using Geant4 is used for the remaining model points for maximum accuracy in the parameter space relevant to the expected sensitivity. In order to account for pileup effects, all signal samples are overlaid with simulated minimum bias events generated using Pythia8 and the A3 tune [182], and reweighted to match the pileup distribution measured in data.

The cross sections for electroweakino pair production have been calculated using Resummino [183] at next-to-leading order (NLO) in the strong coupling constant and including next-to-leading logarithm (NLL) terms in the soft gluon resummation [184, 185].

4.3.2 Background samples

Top pair production and single top processes were generated using Powheg-Box v2 [186], implementing the Powheg method [187, 188] for merging NLO MEs with the PSs. The PS, hadronisation and underlying event were simulated using Pythia8 with the A14 tune. Production of $t\bar{t}$ in association with a vector boson ($t\bar{t} + V$) is generated using MadGraph5_aMC@NLO 2.3.3, interfaced with Pythia8 for the PS. The set of PDFs used for simulation of $t\bar{t}$, single top, and $t\bar{t} + V$ is the NNPDF2.3LO set.

Production of a vector boson V with additional jets ($W/Z + \text{jets}$) is simulated using Sherpa 2.2.1 [130, 189], allowing up to two (four) additional parton emissions at NLO (LO) accuracy. The CKKW ME+PS matching and merging scheme [190, 136] is used, extended to NLO accuracy [191]. Diboson (VV) and multiboson (VVV) processes are simulated using Sherpa 2.2.1 and 2.2.2 with the default Sherpa generator tune. The PDFs used are provided by the NNPDF3.0NNLO set [192].

All Higgs processes are simulated using Powheg-Box v2 for the ME calculations and Pythia8 for the PS, underlying event and hadronisation. While the generation of $h + t\bar{t}$ uses the A14 tune and the NNPDF2.3LO set, $h + V$ and single Higgs production are simulated using the NNPDF 3.0 NNLO set and the AZNLO [193] set of tuned generator parameters.

The detector simulation for all MC background samples was performed using the full detector simulation based on Geant4, introduced in section 2.2.8. Except for the MC samples generated using Sherpa, all background samples use EvtGen v1.2 or v1.6 to model the decay of HF

Table 4.1: Overview of configuration of MC generators used for simulating the various signal and SM background processes.

Process	Matrix element	Parton shower	PDF set	Cross section	Tune
Signal	MadGraph5_aMC@NLO 2.6.2	Pythia 8.230	NNPDF 2.3 LO	NLO+NLL [183–185]	A14
$t\bar{t}$	Powheg-Box	Pythia 8.230	NNPDF2.3LO	NNLO+NNLL [194, 195]	A14
t (s-channel)	Powheg-Box	Pythia 8.230	NNPDF2.3LO	NLO [196]	A14
t (t-channel)	Powheg-Box	Pythia 8.230	NNPDF2.3LO	NLO [196]	A14
$t + W$	Powheg-Box	Pythia 8.230	NNPDF2.3LO	NNLO [196, 197]	A14
$t\bar{t} + V$	MadGraph5_aMC@NLO 2.3.3	Pythia 8.210	NNPDF2.3LO	NLO [198, 199]	A14
V + jets	Sherpa 2.2.1		NNPDF3.0NNLO	NNLO [200]	Sherpa default
VV	Sherpa 2.2.1/2.2.2		NNPDF3.0NNLO	NLO [174]	Sherpa default
VVV	Sherpa 2.2.1/2.2.2		NNPDF3.0NNLO	NLO [174]	Sherpa default
$h + t\bar{t}$	Powheg-Box	Pythia 8.230	NNPDF2.3LO	NLO [201]	A14
$h + V$	Powheg-Box	Pythia 8.212	NNPDF3.0NNLO	NNLO [201]	AZNLO
h *(ggF)*	Powheg-Box	Pythia 8.212	NNPDF3.0NNLO	N^3LO+N^3LL [201]	AZNLO
h *(VBF)*	Powheg-Box	Pythia 8.212	NNPDF3.0NNLO	NNLO [201]	AZNLO

quarks. Similar to the signal models, all background samples are overlaid with simulated minimum bias events generated with Pythia8 and the A3 tune.

4.4 Object definitions

The reconstruction of physics objects requires the combination of data from multiple detector components. Due to finite detector resolutions, and the sheer amount of particles produced in each collision, this process does not always work without flaws. Sometimes, objects are falsely reconstructed or not reconstructed at all. In order to minimise reconstruction errors, different identification and reconstruction criteria are introduced for each physics object category. Electrons and muons are categorised into *baseline* and *signal* objects. Baseline objects have a smaller purity but a higher acceptance which is e.g. useful for the reconstruction of the missing transverse momentum. Stricter identification and isolation criteria are required for signal objects, resulting in lower acceptances but also lower probability of reconstruction errors. In the following, signal-type objects are used as the physical objects. Table 4.2 gives a comprehensive summary of the object definitions introduced in the ensuing sections.

4.4.1 Tracks and vertices

The reconstruction of tracks of charged particles starts with the formation of clusters from raw data recorded in the Pixel and silicon microstip tracker (SCT) detectors. Clusters are formed by grouping together adjacent pixels and strips with energy deposits above a certain threshold and are subsequently used to create three-dimensional space-points, representing the points where charged particles traversed the active inner detector (ID) material [202]. Sets of three space-points form track seeds that serve as inputs for a combinatorial Kalman filtering technique [203] that includes additional space-points from the remaining pixel and SCT layers to extend the preliminary trajectory. A χ^2 track fit is performed at each step of the extension. Where seeds can be extended by more than one compatible space-point in a given layer, multiple track candidates are formed. Ambiguities between candidates are resolved by assigning them a

score taking into account basic track properties like the χ^2 of the track fit, or its associated p_T [202]. The ambiguity solver requires track candidates to contain a minimum of 7 pixel and SCT clusters, have a maximum of one shared pixel cluster and two shared SCT clusters on the same layer and have no more than two holes[†] of which only one is allowed to be in the pixel detector. Track candidates also need to have $p_T > 400\,\mathrm{MeV}$, $|\eta| < 2.5$ and have longitudinal (z_0) and transversal (d_0) impact parameters with respect to their associated vertex satisfying $|z_0 \sin\theta| < 3.0\,\mathrm{mm}$ and $|d_0| < 2.0\,\mathrm{mm}$, where θ is the polar angle of the track [202]. Track candidates surviving the ambiguity solver are extended by compatible hits in the transition radiation tracker (TRT) [204] and subject to a global high-resolution track fit before being added to the final track collection [202].

Vertex reconstruction uses a selection of tracks satisfying a set of quality requirements [205] to fit the best vertex position in a procedure iteratively downweighting less compatible tracks [206]. Once the vertex position has been determined, incompatible tracks with small weights are removed and can be reused for the reconstruction of additional vertices [206]. All reconstructed vertices with at least two associated tracks are kept as valid primary vertex candidates. In events with multiple candidates, the primary vertex is defined to be the one with the highest $\sum p_T^2$ of its associated tracks.

4.4.2 Electrons and Photons

Electron and photon candidates are reconstructed from energy deposits in topologically connected cells in the electromagnetic and hadronic calorimeters. The reconstruction algorithm starts with the preparation of the energy deposits into so-called *topo-clusters* [207]. These are formed by calorimeter cells containing energy deposits above a certain noise threshold, so-called *seed* cells, including their neighbouring cells which, in turn, can also act as seed cells. All cell signals are measured at the electromagnetic scale, assuming that energy deposits stem only from electromagnetic interactions. Although the topo-clustering algorithm starts with cells from both calorimeters, only energies from cells in the Electromagnetic (EM) calorimeter are used in the subsequent electron and photon reconstruction steps [208]. Using only EM topo-clusters with a certain threshold ratio of the EM energy to the total cluster energy significantly reduces contamination from pileup clusters [208]. The EM topo-clusters are then loosely matched to ID tracks that are re-fitted in order to account for energy losses through bremsstrahlung [208]. Vertices from photon conversions are reconstructed from tracks matched to fixed-size clusters [209] and also matched to the EM topo-clusters. In the final step of the reconstruction algorithm, EM topo-clusters are sorted according to descending E_T and tested as seed clusters for dynamic, variable-size *superclusters*, with different seed requirements for electrons and photons [208]. Clusters near seed candidates can be added as satellite cluster candidates, originating e.g. from bremsstrahlung. Electrons and photons are then finally built from the reconstructed superclusters and their energies are calibrated using $Z \to ee$ decays [208].

The identification of prompt electrons relies on a likelihood discriminant built from quantities measured in the ID and calorimeters. The quantities are chosen according to their ability to discriminate prompt isolated electrons from non-prompt leptons originating in e.g. HF decays, from photon conversions or from jets. They include the properties of the electron track, the shape of the EM shower and the quality of the match between the electron track and

---

[†] Holes are intersections of the track trajectory with sensitive detector material not containing a cluster.

the calorimeter clusters [210]. Photon identification, on the other hand, relies on a cut-based selection exploiting the shape of the EM shower [208].

In this analysis, electrons are required to satisfy $p_{\mathrm{T}} > 7\,\mathrm{GeV}$ and $|\eta| < 2.47$. Baseline electrons are identified using the *LooseAndBLayer* requirement on the identification likelihood, requiring a hit in the innermost layer of the pixel detector, at least two additional hits in the remaining layers of the pixel detector and seven hits in the pixel and SCT detectors combined [210]. In addition, the longitudinal impact parameter z_0 of baseline electrons needs to satisfy $\Delta z_0 \sin\theta < 0.5\,\mathrm{mm}$ with respect to the primary vertex. The *LooseAndBLayer* identification yields an average efficiency of about 93%, increasing from low to high electron E_{T} [210]. Signal electrons are a subset of baseline electrons and need to satisfy the *Tight* likelihood identification, yielding an efficiency of 80% for prompt electrons with $E_{\mathrm{T}} = 40\,\mathrm{GeV}$ [210]. In addition to the longitudinal impact parameter, signal leptons also need to satisfy $d_0/\sigma_{d_0} < 5$, where the transverse impact parameter d_0 and its uncertainty σ_{d_0} are measured with respect to the beam line.

Finally, electrons need to be *isolated*, meaning that their vicinity must be clear of additional significant detector activity. Requiring electrons to be isolated prevents the selection of non-prompt electrons originating e.g. from HF decays or misidentifications of light hadrons. Isolation is quantified using two observables, one using tracking information and the other one using calorimeter data. The tracking based isolation variable $p_{\mathrm{T}}^{\mathrm{varcone20}}$ is the sum of all track momenta above $1\,\mathrm{GeV}$ (excluding the electrons track itself) in a cone around the electron. The size of the cone is chosen to be $\Delta R = \min(10\,\mathrm{GeV}/p_{\mathrm{T}}, 0.2)$, i.e. is shrinking with increasing transverse momentum of the electron. The calorimeter based variable $E_{\mathrm{T}}^{\mathrm{cone20}}$ corresponds to the sum of the transverse energies in topo-clusters (excluding the electrons itself and after correcting for pileup effects) in a cone with $\Delta R = 0.2$ around the electrons. In this analysis, both baseline and signal electrons are required to satisfy the *Loose* working point [208], corresponding to the requirements $p_{\mathrm{T}}^{\mathrm{varcone20}}/p_{\mathrm{T}} < 0.2$ and $E_{\mathrm{T}}^{\mathrm{cone20}} < 0.15$. In order to improve the rejection of non-prompt electrons at high transverse momenta, electrons with $p_{\mathrm{T}} > 200\,\mathrm{GeV}$ need to satisfy the *HighPtCaloOnly* working point, applying the tighter requirement $E_{\mathrm{T}}^{\mathrm{cone20}} < \max(0.015 \cdot p_{\mathrm{T}}, 3.5\,\mathrm{GeV})$.

Photons are required to have $p_{\mathrm{T}} > 13\,\mathrm{GeV}$ and $|\eta| < 2.37$ and need to satisfy the *Tight* identification and *FixedCutTight* isolation requirements introduced in Ref. [208]. In this analysis, photons are only used in the calculation of the missing transverse momentum.

4.4.3 Muons

The reconstruction of muons uses primarily data from the ID and muon spectrometer (MS) and is based on the fact that muons are minimum ionising particles. Muon candidates are independently reconstructed in the ID and the MS as muon tracks and only then combined to a muon candidate that can be used by physics analysis [211, 212]. The track reconstruction in the ID follows the same procedure used for other charged-particle tracks, described in section 4.4.1. In the MS, the muon track reconstruction starts with the identification of short straight-line track segments. Segments from different MS layers are combined into preliminary muon track candidates if they are loosely compatible with the interaction point (IP) and match a first-order approximation of the parabolic trajectory describing the muon track in the magnetic field. Track candidates are then fitted in a global χ^2 fit, taking into account possible MS chamber misalignments as well as interactions with the detector material [212]. In order to increase the reconstruction performance, MS muon tracks are subsequently combined with the ID tracks

using five different reconstruction strategies, described in detail in Ref. [212]. Only two of these strategies are relevant for this analysis:

- *combined muons*, formed by combining the ID and MS tracks through a global fit, taking into account the energy loss in the calorimeters,

- *MS extrapolated muons*, built using MS muon tracks only, but extrapolating the tracks back to the IP and requiring them to be loosely compatible with the IP. Extrapolated muons are mainly used for providing acceptance in the region $2.5 < |\eta| < 2.7$, which is beyond the coverage provided by the ID.

After resolving the overlaps between the different muon types, the muon objects used for physics analysis are subject to a momentum calibration using data from $J/\Psi \to \mu\mu$ and $Z \to \mu\mu$ decays [211, 212].

Identification of muons is performed using quality requirements designed to suppress non-prompt muons originating from pion and kaon decays and allow a robust momentum measurement. Muons in this analysis are built using combined and extrapolated muons that satisfy the *Medium* identification requirements [211]. Combined muons need to have at least three hits in at least two Monitored Drift Tube (MDT) layers, except for the region with $|\eta| < 0.1$, where a single MDT layer is enough, as long as there is no more than one MDT hole layer [212]. Extrapolated muons need to have at least three hits in at least three MDT and Cathode Strip Chamber (CSC) layers [212]. In addition, all muons need to have a significance of the ratio of the measured charge and momentum satisfying $\sigma(q/p) < 7$. Identification of muons with the *Loose* identification working point is evaluated in a $t\bar{t}$ MC sample and yields an efficiency of more than 98% for muons with $p_T > 5\,\mathrm{GeV}$ [212]. The light-hadron rejection rate is roughly 98 for low-p_T muons with $p_T < 20\,\mathrm{GeV}$, and decreases with increasing muon p_T, reaching 830 for muons with $p_T > 100\,\mathrm{GeV}$ [212].

Baseline muons in this analysis also need to satisfy $p_T > 6\,\mathrm{GeV}$ and $|\eta| < 2.7$. The longitudinal impact parameter of baseline muons with respect to the primary vertex is required to be $\Delta z_0 \sin\theta < 0.5\,\mathrm{mm}$. Signal muons additionally need to be within $|\eta| < 2.5$ and have a transverse impact parameter satisfying $d_0/\sigma_{d_0} < 3$. Similar to electrons, muons also need to be isolated, using the same variables used for electron isolation. Both signal and baseline muons need to conform to the *Loose* working point, requiring $p_T^{\mathrm{varcone20}}/p_T < 0.3$ and $E_T^{\mathrm{cone20}} < 0.15$ [212]. The *Loose* isolation working point yields an efficiency rapidly increasing from 86% for muons with $5\,\mathrm{GeV} < p_T < 20\,\mathrm{GeV}$ to 97% for muons with $20\,\mathrm{GeV} < p_T < 100\,\mathrm{GeV}$. Muons with $p_T > 100\,\mathrm{GeV}$ have an isolation efficiency of more than 99% [212]. The rejection rate for muons from HF decays ranges from 14 to 8 with increasing p_T in the range relevant for this search [212].

4.4.4 Jets

Jets are reconstructed at the EM scale using the anti-k_t algorithm [213] with a radius parameter $R = 0.4$, implemented in the FASTJET [214, 215] package. The inputs to the anti-k_t algorithm are topo-clusters [216], built using the procedure introduced in section 4.4.2. Tracks with $p_T > 500\,\mathrm{MeV}$ and an association to the primary vertex are assigned to jets using *ghost association* [217], a method treating them as particles with infinitesimal momentum such that the properties of the calorimeter-based jets are not changed.

Reconstructed jets undergo a jet energy scale (JES) calibration, correcting the four-momentum and scaling the energy and mass [216]. In a first step, energy contributions from in-time and out-of-time pileup are removed using a data-driven jet-by-jet approach based on jet areas and pileup p_T density. Additionally, a residual correction derived from MC simulation and parameterised by the number of mean interactions per bunch crossing and the number of reconstructed primary vertices is applied [216, 217]. The reconstructed jet four-momentum is corrected to the particle-level energy scale through an absolute JES and η calibration. In order to reduce the dependence of the jet response (i.e. the ratio between the measured jet energy and the true jet energy) on the flavour and energy distribution of its constituents, a series of multiplicative corrections, called global sequential calibration (GSC) [218], is applied. The GSC improves the jet energy resolution (JER) and is based on data from the calorimeters, jet-related tracking information as well as MS information. Differences between the jet response in data and MC simulation, caused by imperfect detector and physics simulations, are corrected using so-called *in situ* calibrations [216]. The jet response in data and MC simulations is measured separately, allowing to derive a correction factor that is applied on data. Similar to the JES, the JER is also calibrated. Its calibration is performed using p_T asymmetry measurements in dijet events [219].

Even after the subtraction of pileup effects, some pileup jets still remain. The jet vertex tagger (JVT) [220], a multivariate discriminant, can be used to suppress pileup jets. It is based on variables that describe the fraction of the total jet momentum corresponding to tracks associated to the primary vertex. In this analysis, jets with $p_T < 120\,\text{GeV}$ and $|\eta| < 2.5$ need to be associated to the primary vertex using the *medium* working point, achieving an average 92% efficiency for jets originating from the hard scatter interaction [216].

Baseline jets in this analysis are required to have $p_T > 20\,\text{GeV}$ and $|\eta| < 4.5$. Analysis variables built using jets use signal-level jets with $p_T > 30\,\text{GeV}$ and $|\eta| < 2.8$.

4.4.5 Flavour tagging

As can be seen through the Cabibbo–Kobayashi–Maskawa (CKM) matrix, b-quarks primarily decay through $b \to Wc$. However, due to the small coupling constant proportional to the corresponding CKM matrix element V_{cb} (corresponding to the $b \leftrightarrow c$ transition), b-hadrons have relatively long lifetimes of the order of $1.5\,\text{ps}$ ($\langle c\tau \rangle \approx 450\,\mu\text{m}$) [7]. In the typical momentum ranges, b-hadrons can have a measurable flight length before decaying, leading to secondary vertices that are displaced from the hard-scatter interaction point. In order to exploit this, ATLAS uses a collection of algorithms designed to discern HF jets containing b-hadrons from light-flavour jets by exploiting either the impact parameters or reconstructing the displaced vertices. A multivariate classifier, called MV2 [221] combines the outputs of the different taggers using a boosted decision tree (BDT) algorithm that is trained on $t\bar{t} + Z'$ MC samples.

Due to the Higgs decay $h \to b\bar{b}$ in the signal model targeted, b-jets play a crucial role in the analysis. Baseline jets with $|\eta| < 2.5$ are used as input to the MV2c10 b-tagging algorithm, an implementation of the MV2 discriminant using a c-jet fraction of 7% during the BDT training [222, 223]. The working point chosen for the MV2c10 tagger achieves a b-tagging efficiency of 77% with a rejection rates of 4.9, 15, and 110 for c-jets, τ-jets and light-flavour jets, respectively, measured in simulated $t\bar{t}$ events [222].

4.4.6   Missing transverse momentum

Momentum conservation in the transverse plane implies that the sum of the transverse momenta of all objects in a *pp* collision should vanish. Particles escaping the detector without being measured thus lead to a momentum imbalance, in the following referred to as missing transverse momentum $\boldsymbol{p}_\mathrm{T}^\mathrm{miss}$ with magnitude $E_\mathrm{T}^\mathrm{miss}$. The missing transverse momentum in each event is computed using all reconstructed objects and takes into account tracks associated to the primary vertex but not used for any reconstructed objects [224], yielding

$$\boldsymbol{p}_\mathrm{T}^\mathrm{miss} = -\sum \boldsymbol{p}_\mathrm{T}^e - \sum \boldsymbol{p}_\mathrm{T}^\gamma - \sum \boldsymbol{p}_\mathrm{T}^\mu - \sum \boldsymbol{p}_\mathrm{T}^\mathrm{jet} - \sum \boldsymbol{p}_\mathrm{T}^\mathrm{track}. \tag{4.1}$$

While terms originating from the reconstructed, calibrated objects are collectively referred to as the *hard term*, the remaining track term is referred to as *soft term*. As τ-leptons are not explicitly reconstructed in this analysis, no corresponding term is included in eq. (4.1). Hadronic decays of τ-leptons are, however, included in the jet term as they are, in general, reconstructed as jets. The computation of $E_\mathrm{T}^\mathrm{miss}$ uses all baseline objects introduced in the previous sections. Ambiguities between objects are resolved using an overlap removal procedure [224] that is separate and independent from the procedure described in section 4.5. In order to reduce effects from pileup, the $E_\mathrm{T}^\mathrm{miss}$ is computed using the *Tight* working point described in Ref. [225], excluding forward jets with $|\eta| > 2.4$ and $p_\mathrm{T} < 30\,\mathrm{GeV}$.

Events without any true $E_\mathrm{T}^\mathrm{miss}$ can have non-zero reconstructed $E_\mathrm{T}^\mathrm{miss}$ due to residual pileup effects, object mismeasurements or particles escaping through uninstrumentalised regions of the detector. Such *fake* $E_\mathrm{T}^\mathrm{miss}$ allows events without any real $E_\mathrm{T}^\mathrm{miss}$ (e.g. $Z(\to ee) + \mathrm{jets}$) to pass the event selection criteria and end up in the kinematic regions of interest even after requiring a certain threshold value of $E_\mathrm{T}^\mathrm{miss}$.

4.5   Overlap removal

As the reconstruction procedure runs independently for each object type, it may happen that the same tracks or energy deposits in the calorimeters are used for the reconstruction of two different objects. For example, electrons tend to cluster as well as jets and are therefore often also reconstructed as electron-seeded jets [226]. In order to resolve ambiguities and prevent double-counting, an overlap removal procedure using the distance parameter $\Delta R_y = \sqrt{(\Delta y)^2 + (\Delta \phi)^2}$ is performed. The procedure sequentially runs the following steps on baseline objects, with only surviving objects participating in subsequent steps:

1. Electrons sharing an ID track with a muon are removed, preventing duplication of muons as electrons via bremsstrahlung with subsequent photon conversion [226].

2. Jets within $\Delta R_y < 0.2$ of an electron are rejected, preventing the pure duplication of electrons as electron-seeded jets [226].

3. Electrons overlapping with remaining jets within $\Delta R_y = \min(0.4, 0.04 + 10\,\mathrm{GeV}/p_\mathrm{T})$ are removed, resolving the regime where hadronic jets lose a fraction of their energy to electron-seeded jets [226]. The shrinking cone size avoids unnecessary rejection of electrons originating from decays of boosted particles together with jets.

Table 4.2: Overview of the object definitions used in the analysis.

Property	Baseline type	Signal type
Electrons		
Kinematic	$p_\mathrm{T} > 7\,\mathrm{GeV}$, $|\eta| < 2.47$	$p_\mathrm{T} > 7\,\mathrm{GeV}$, $|\eta| < 2.47$
Identification	*LooseAndBLayer* [210]	*Tight* [210]
Impact parameters	$\Delta z_0 \sin\theta < 0.5\,\mathrm{mm}$	$\Delta z_0 \sin\theta < 0.5\,\mathrm{mm}$, $d_0/\sigma_{d_0} < 5$
Isolation	–	*Loose* [208] ($p_\mathrm{T} \leq 200\,\mathrm{GeV}$)
		HighPtCaloOnly [208] ($p_\mathrm{T} > 200\,\mathrm{GeV}$)
Muons		
Kinematic	$p_\mathrm{T} > 6\,\mathrm{GeV}$, $|\eta| < 2.7$	$p_\mathrm{T} > 6\,\mathrm{GeV}$, $|\eta| < 2.5$
Identification	*Medium* [211]	*Medium* [211]
Impact parameters	$\Delta z_0 \sin\theta < 0.5\,\mathrm{mm}$	$\Delta z_0 \sin\theta < 0.5\,\mathrm{mm}$, $d_0/\sigma_{d_0} < 3$
Isolation	–	*Loose* [212]
Jets		
Kinematic	$p_\mathrm{T} > 20\,\mathrm{GeV}$, $|\eta| < 4.5$	$p_\mathrm{T} > 30\,\mathrm{GeV}$, $|\eta| < 2.8$
JVT	–	*Medium* [216], $p_\mathrm{T} < 120\,\mathrm{GeV}$, $|\eta| < 2.5$
b-jets		
Kinematic	$p_\mathrm{T} > 20\,\mathrm{GeV}$, $|\eta| < 4.5$	$p_\mathrm{T} > 30\,\mathrm{GeV}$, $|\eta| < 2.5$
JVT	–	*Medium* [216], $p_\mathrm{T} < 120\,\mathrm{GeV}$, $|\eta| < 2.5$
b-tagging	–	MV2c10 [222] with 77% efficiency

4. Jets with less than three associated tracks, within $\Delta R_y < 0.2$ of a muon or where the muon has been matched to the jet through ghost association [227] are removed. This resolves for example scenarios where a muon is reconstructed as a jet due to bremsstrahlung or final state radiation (FSR) with subsequent photon conversion reconstructed both as electron and jet [226].

5. Muons overlapping with a remaining jet are removed. The same shrinking cone size as for electrons is used. This predominantly removes non-prompt muons produced in light meson or HF decays together with jets [226].

4.6   Analysis variables

In order to separate supersymmetric signal events from SM processes, it is necessary to apply requirements on different discriminating observables, creating so-called *signal regions* enriched in signal events. In addition, these variables are also used to construct regions enriched in SM background events, in the following used for the background estimation in the signal regions. The distributions of all discriminating variables obtained from MC simulation are illustrated in fig. 4.3, comparing signal and SM background distributions. Both are normalised to unity in order to highlight their differences in shape. Most observables show at least some dependence on the absolute mass scale of the supersymmetric particles, as well as the mass difference between $\tilde{\chi}_1^\pm/\tilde{\chi}_2^0$ and $\tilde{\chi}_1^0$, resulting in different different shapes for different signal points.

Number of jets

The simplified model depicted in fig. 4.1 features two b-jets in the final state, originating from the decay of the Higgs boson. In the following, all events are thus required to have exactly two b-jets in the final state, significantly reducing contributions from e.g. W + jets processes that have a relatively low probability of producing two b-jets. In order to avoid rejecting signal events with initial state radiation (ISR) or FSR (as e.g. in fig. 2.8), a third, light-flavour jet is allowed in the final state.

Invariant mass of the *b*-tagged jets

The invariant mass of the two b-jets $m_{b\bar{b}}$ can be defined using the well-known energy-momentum relation,

$$m_{b\bar{b}}^2 = (\mathbf{P}_{b_1} + \mathbf{P}_{b_2})^2 = m_{b_1}^2 + m_{b_2}^2 + 2\left(E_{b_1} E_{b_2} - \boldsymbol{p}_{b_1} \boldsymbol{p}_{b_2}\right) \tag{4.2}$$

where $\mathbf{P}_{b_1}$ and $\mathbf{P}_{b_2}$ are the four-vector momenta of the leading and subleading b-jets, respectively. The term *leading* henceforth refers to the object with the largest p_{T} in its object category. In the high-relativistic limit $E \gg m$, the invariant mass of the two b-jets can be written as

$$m_{b\bar{b}} = \sqrt{2 p_{\mathrm{T}}^{b_1} p_{\mathrm{T}}^{b_2} (\cosh \Delta \eta_{bb} - \cos \Delta \phi_{bb})}, \tag{4.3}$$

where $\Delta \eta_{bb}$ and $\Delta \phi_{bb}$ are the differences in pseudorapidity and azimuthal angle between the two b-jets, respectively.

As the two b-jets originate from the Higgs decay $h \to b\bar{b}$, their measured invariant mass will in general be close to the measured Higgs mass of around 125 GeV [7], leading to a peak in the $m_{b\bar{b}}$ distribution, as can clearly be seen in fig. 4.3(d). In most SM background processes relevant to the search, the b-jets do not originate from a Higgs decay, and thus their $m_{b\bar{b}}$ distribution does not exhibit the same peak-like structure. In order to enrich signal events in a selection, $m_{b\bar{b}}$ will be required to be close to the Higgs mass in the following.

Missing transverse energy

The missing transverse energy $E_{\mathrm{T}}^{\mathrm{miss}}$ is an observable finding widespread usage in searches for SUSY at the LHC. In SM processes, $E_{\mathrm{T}}^{\mathrm{miss}}$ only stems from neutrinos and fake $E_{\mathrm{T}}^{\mathrm{miss}}$ arising e.g. from mismeasurements or imperfect detector hermeticity. In the case of the SUSY scenario considered in the following, two lightest supersymmetric particles (LSPs) escape the detector, leaving a considerable amount of missing transverse momentum, such that a lower requirement on $E_{\mathrm{T}}^{\mathrm{miss}}$ allows to separate signal and background processes. Figure 4.3(c) shows the $E_{\mathrm{T}}^{\mathrm{miss}}$ distribution, illustrating the fact that signal models with high absolute sparticle masses as well as high mass differences tend to have the largest $E_{\mathrm{T}}^{\mathrm{miss}}$.

Transverse mass

The transverse masse m_{T} [228, 229] is one of the most important observables considered in this analysis. It aims to reconstruct the mass of a heavy particle decaying into two daughter

particles subject to a co-linear boost in the laboratory transverse plane. In SUSY searches targeting the 1-lepton final state, m_T is commonly used to reconstruct the transverse mass of the W boson decaying into a lepton–neutrino pair, and is therefore defined as

$$m_\mathrm{T} = \sqrt{2p_\mathrm{T}^\ell E_\mathrm{T}^\mathrm{miss}(1 - \cos[\Delta\phi(\boldsymbol{p}_\mathrm{T}^\ell, \boldsymbol{p}_\mathrm{T}^\mathrm{miss})])}, \tag{4.4}$$

where $\boldsymbol{p}_\mathrm{T}^\ell$ is the momentum three-vector of the lepton in the event. As events with additional leptons are vetoed, the vast majority of the leptons in background processes stem from leptonic decays of W bosons. In background events where the neutrino from $W \to \ell\nu$ is the only source of $E_\mathrm{T}^\mathrm{miss}$, the transverse mass has a theoretical kinematic endpoint at the W boson mass,

$$m_\mathrm{T}^\mathrm{max} = m_W \approx 80\,\mathrm{GeV}. \tag{4.5}$$

Due to finite detector resolution, mismeasurements or additional $E_\mathrm{T}^\mathrm{miss}$ in the event, background events can sometimes have $m_\mathrm{T} > m_W$, leading to a kinematic endpoint at m_W that is not infinitely sharp.

In the signal scenarios considered in the analysis, the LSPs constitute a majority of the $E_\mathrm{T}^\mathrm{miss}$ in an event, which typically leads to a m_T distribution that is significantly broader than that of background processes and does not present the same kinematic endpoint. A lower requirement on the transverse mass slightly above the W boson mass thus allows to reject a majority of the SM background events while largely unaffecting the signal distribution. As can be seen in fig. 4.3(c),the broadness of the m_T distribution depends on the scale of the signal mass parameters, with increasing mass differences leading to increasingly broad distributions. For this reason, different signal regions with varying requirements on m_T can be constructed, targeting different kinematic regimes in the signal grid. The optimisation of multiple signal regions will be discussed in chapter 5.

Contransverse mass

The contransverse mass m_CT [230] is designed to have a kinematic endpoint for pair produced heavy particles decaying into invisible and visible particles subject to a contra-linear boost. In the following, m_CT is defined as

$$m_\mathrm{CT} = \sqrt{2p_\mathrm{T}^{b_1} p_\mathrm{T}^{b_2}(1 + \cos\Delta\phi_{bb})}, \tag{4.6}$$

where $p_\mathrm{T}^{b_1}$ and $p_\mathrm{T}^{b_2}$ are the transverse momenta of the two b-jets in the final state. Although m_CT is invariant under co-linear boosts in the beam direction[†], it is not invariant under transverse boosts, e.g. due to ISR jets, such that m_CT as well as its kinematic endpoint depend on the size and direction of the transverse boost. For this reason, a boost-corrected version of the contransverse mass is used in the following. The correction algorithm is described in detail in Ref. [231] and uses an estimate of the energy of the upstream pair-produced heavy particles to boost the four-momenta of the visible decay products back into the centre-of-mass frame of the pair-produced particles. The approach provides a conservative value of m_CT that is always

---

[†]   This is by construction the case, as only transverse quantities are used to compute m_CT.
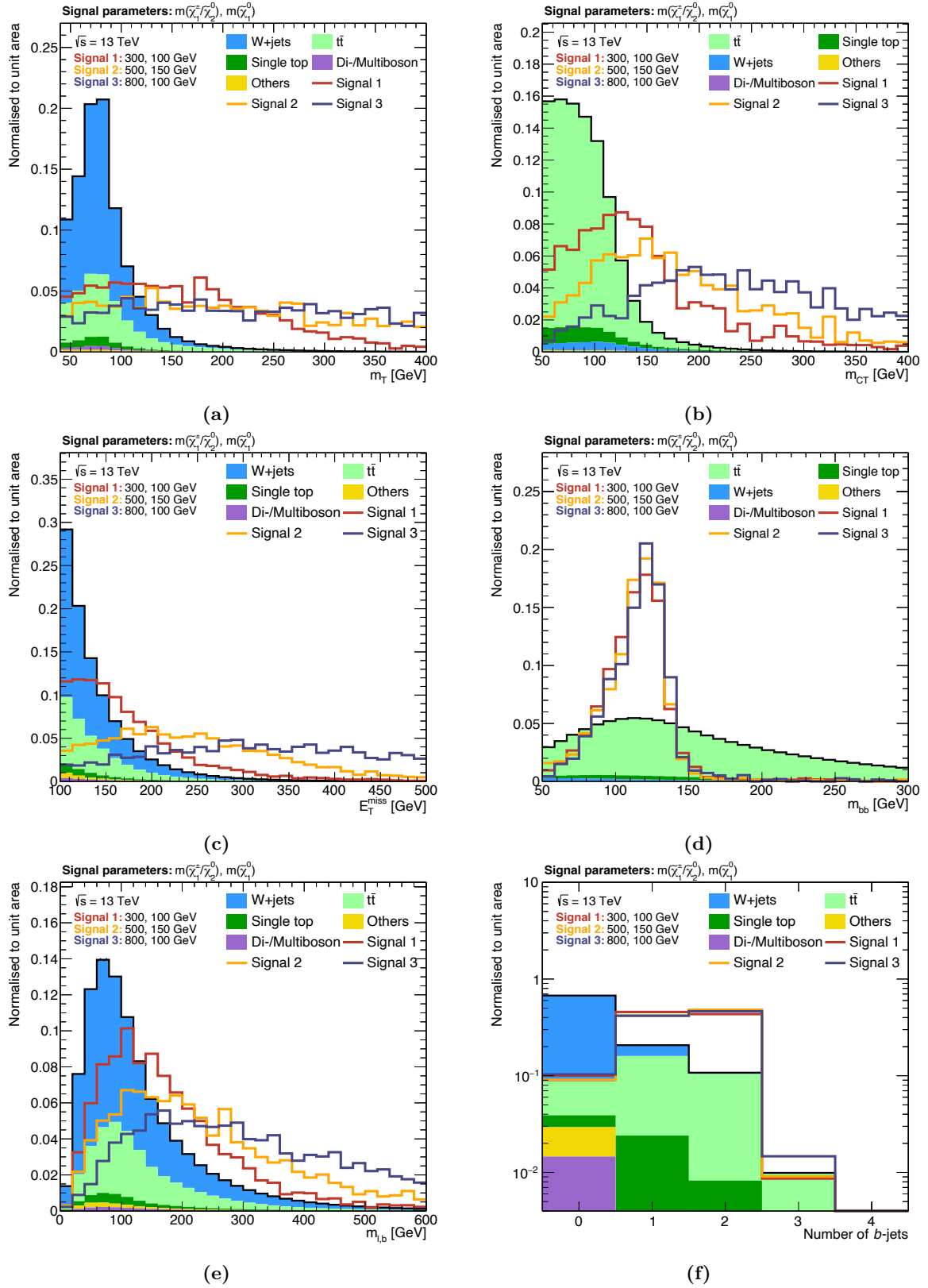
Figure 4.3: Distributions of the most important observables used in the analysis. The simulated SM backgrounds are stacked on top of each other, and distributions from exemplary signal models with the quoted mass parameters are overlaid. In order to emphasise the shape differences, both background and signal distributions are normalised to unity. A preselection of exactly one lepton (signal and baseline), at least two jets and $E_T^{miss} > 100\,\text{GeV}$ is applied.

smaller than the true m_{CT} value measured in the centre-of-mass frame of the pair-produced particles.

For $t\bar{t}$ events where each top quark decays via $t \to bW$, the two b-jets used for calculating m_{CT} stem from each of the two decay branches of the $t\bar{t}$ system. It can be shown [231] that, in this case, the boost-corrected contransverse mass has a kinematic endpoint at

$$m_{\mathrm{CT}}^{\max} = \frac{m^2(t) - m^2(W)}{m(t)} \approx 135\,\mathrm{GeV}. \tag{4.7}$$

In signal events, the two input b-jets originate from the same Higgs boson, and thus m_{CT} does not exhibit a kinematic endpoint but rather tends to take much higher values. Figure 4.3(b) clearly illustrates the kinematic endpoint for $t\bar{t}$ backgrounds and further shows that signal distributions take on much higher values depending on their mass parameter scales. Similar as for the transverse mass, varying lower bounds on m_{CT} will be used in chapter 5 to define signal regions optimised to different kinematic regimes.

Invariant mass of the lepton and leading *b*-jet

The invariant mass of the lepton and the leading b-jet, $m_{\ell b_1}$, is designed to offer high rejection power towards $t\bar{t}$ and single top processes. In events where the lepton and leading b-jet originate from the same top quark decay $t \to bW \to b\ell\nu$, the $m_{\ell b_1}$ distribution has a kinematic endpoint at

$$m_{\ell b_1}^{\max} = \sqrt{m^2(t) - m^2(W)} \approx 153\,\mathrm{GeV} \tag{4.8}$$

In signal events, the lepton and leading b-jet originate from the decay chains of the $\tilde{\chi}_1^\pm$ and $\tilde{\chi}_2^0$, respectively and thus the $m_{\ell b_1}$ distribution depends on the mass scale of the SUSY particles, yielding especially good discriminative power especially for signal scenarios with high $\tilde{\chi}_1^\pm/\tilde{\chi}_2^0$ masses.

4.7 Trigger strategy

The trigger strategy of an analysis is crucial to select *pp* events worth investigating, and typically relies on triggers sensitive to physics objects that are important to the considered signal scenarios. The data used in this analysis have been recorded with $E_{\mathrm{T}}^{\mathrm{miss}}$ triggers. Selecting events with invisible particles is inherently difficult precisely because these particles do not leave a trace in the detector. Like offline analysis, the trigger algorithms thus have to infer the $E_{\mathrm{T}}^{\mathrm{miss}}$ from the momenta of the visible particles, but have to satisfy the stringent online constraints set by the high-luminosity environment of the LHC.

As described in section 2.2.7, the Level 1 (L1) trigger uses only parts of the instrumented regions, a technique that is not well suited for momentum imbalance triggers that rely on a sum of momenta over the full solid angle [232]. In the L1 trigger, dedicated hardware sums the signals from calorimeter cells into *towers* with a granularity matching that of the calorimeter. Towers of calorimeter cells exceeding a certain threshold are used to generate larger towers with coarser granularity, the x and y projections of which are subsequently summed to get an estimate of $E_{\mathrm{T}}^{\mathrm{miss}}$ in the event. The tower thresholds are varied such that trigger rates are

provided during the different data-taking periods. Finally, the L1 triggers used in this analysis employed a threshold of $E_T^{\mathrm{miss}} > 50 \,\mathrm{GeV}$, before feeding passing events to the High Level Trigger (HLT) for further analysis.

Two different types of E_T^{miss} triggers are used by the HLT, one based on jets (`mht` algorithm), and one implementing local pile-up suppression (`pufit` algorithm). As hadronic jets dominate the visible momentum in most interesting events, using them for E_T^{miss} computation and triggering is well-motivated. The `mht` algorithm was used during the 2015–2016 data taking period and computes the E_T^{miss} from the negative vectorial sum of the transverse momenta of all jets with a transverse momentum $p_T > 7 \,\mathrm{GeV}$ before calibration [232]. The HLT jets are reconstructed and calibrated using a similar procedure as for offline analysis, and are thus corrected for pile-up effects [233]. The `pufit` algorithm was used during the 2017–2018 data taking period and takes as input topo clusters formed using the method described in section 4.4.2. The clusters are subsequently combined into η–ϕ patches of approximately jet size and corrected for pile-up effects based on the distribution of the energy deposits in the calorimeter. The `pufit` algorithm assumes that high E_T deposits stem from the hard-scatter events, while low E_T deposits originate mostly from pile-up effects [232]. The online E_T^{miss} threshold used increased from $70 \,\mathrm{GeV}$ to $110 \,\mathrm{GeV}$ in order to keep the trigger rate more or less stable under rising instant luminosities during the different data-taking periods.

Since the online reconstruction techniques used by the triggers are slightly different[†] than those used in offline physics analysis, the performance of triggers is in general not a simple step function but consists a so-called *turn-on curve* with rising efficiency, followed by a *plateau region* with constant efficiency. In order to achieve the same trigger selection in MC as in data, the MC events are each assigned a random run number that are distributed according to the respective integrated luminosities of each data taking period. Using the run numbers, the same triggers used for data-taking during each run can be applied for MC events.

Figure 4.4 shows the combined E_T^{miss} trigger efficiencies for the electron and muon channel separately. In the following, an offline requirement of $E_T^{\mathrm{miss}} > 240 \,\mathrm{GeV}$ is applied for all analysis regions, selecting events where the E_T^{miss} triggers are fully efficient and no significant difference between MC and data is observed. Thus, no trigger efficiency correction is considered in the following. A statistical uncertainty of 2% is used to account for the difference between data and MC in the trigger plateaus.

4.8 Event cleaning

Before being considered for analysis, events need to pass a series of quality requirements. Data events need to be certified to be good for physics analysis by the ATLAS data quality system [234], requiring that no transient detector issues have compromised the quality of the data events recorded. Losses in data quality could happen due to e.g. high-voltage trips in detector components or noise bursts in the detector electronics [234]. Only data events are considered where all detector components were flagged as being operational, a process that is performed at the granularity of a *luminosity block*—a time period of roughly $60 \,\mathrm{s}$ of data-taking where the instantaneous luminosity, detector and trigger configuration are considered to be constant.

[†]   This is necessary to be able to handle the substantial data streams caused by large rate of pp collisions.

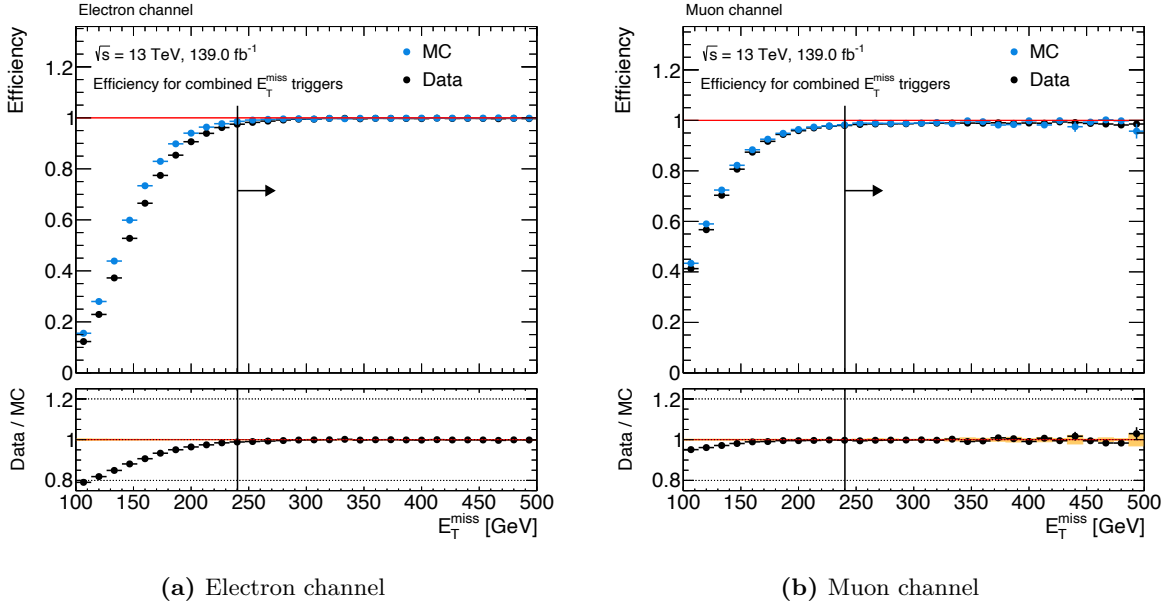**(a)** Electron channel   **(b)** Muon channel

Figure 4.4: Efficiencies of the combined E_T^{miss} triggers in data and MC events, triggered by single lepton triggers in the (a) electron and (b) muon channels. A preselection requiring exactly one lepton (baseline and signal), at least two jets, and $E_T^{miss} > 100\,\text{GeV}$ is applied on all events. The arrow indicates the offline E_T^{miss} requirement applied on all selections in the analysis.

A second series of quality requirements is applied on both data and MC events. To be considered in any subsequent analysis step, events need to have at least one reconstructed primary vertex with a minimum of two tracks with $p_T > 500\,\text{MeV}$ associated to it. Events are discarded where a jet is tagged as originating from a non-collision background process. The `Loose` working point described in Ref. [235] is used to tag such jets, yielding an efficiency of 99.5% for jets from pp collision events with $p_T > 20\,\text{GeV}$. Similarly, events are rejected if they contain a *bad* muon with a significantly worse than usual momentum resolution that can affect many variables in the entire event and therefore may have non-negligible effects on the analysis. In the following, muons are flagged as *bad* if the relative error on the combined q/p measurement is either larger than 0.2 or worse than the one from the individual ID and MS track fits. Events are also rejected if a reconstructed muon is flagged to originate from cosmic radiation, using thresholds on the transverse and longitudinal impact parameters of $d_0 > 0.2\,\text{mm}$ and $z_0 > 1\,\text{mm}$ with respect to the primary vertex.

Bibliography

[1] I. C. Brock and T. Schorner-Sadenius, *Physics at the terascale*. Wiley, Weinheim, 2011. https://cds.cern.ch/record/1354959.

[2] M. E. Peskin and D. V. Schroeder, *An Introduction to quantum field theory*. Addison-Wesley, Reading, USA, 1995. http://www.slac.stanford.edu/~mpeskin/QFT.html.

[3] S. P. Martin, "A Supersymmetry primer," `arXiv:hep-ph/9709356 [hep-ph]`. [Adv. Ser. Direct. High Energy Phys.18,1(1998)].

[4] M. Bustamante, L. Cieri, and J. Ellis, "Beyond the Standard Model for Montaneros," in *5th CERN - Latin American School of High-Energy Physics*. 11, 2009. `arXiv:0911.4409 [hep-ph]`.

[5] L. Brown, *The Birth of particle physics*. Cambridge University Press, Cambridge Cambridgeshire New York, 1986.

[6] P. J. Mohr, D. B. Newell, and B. N. Taylor, "CODATA Recommended Values of the Fundamental Physical Constants: 2014," *Rev. Mod. Phys.* **88** no. 3, (2016) 035009, `arXiv:1507.07956 [physics.atom-ph]`.

[7] P. D. Group, "Review of Particle Physics," *Progress of Theoretical and Experimental Physics* **2020** no. 8, (08, 2020) , https://academic.oup.com/ptep/article-pdf/2020/8/083C01/34673722/ptaa104.pdf. https://doi.org/10.1093/ptep/ptaa104. 083C01.

[8] **Super-Kamiokande** Collaboration, Y. Fukuda *et al.*, "Evidence for oscillation of atmospheric neutrinos," *Phys. Rev. Lett.* **81** (1998) 1562–1567, `arXiv:hep-ex/9807003 [hep-ex]`.

[9] Z. Maki, M. Nakagawa, and S. Sakata, "Remarks on the unified model of elementary particles," *Prog. Theor. Phys.* **28** (1962) 870–880. [,34(1962)].

[10] N. Cabibbo, "Unitary symmetry and leptonic decays," *Phys. Rev. Lett.* **10** (Jun, 1963) 531–533. https://link.aps.org/doi/10.1103/PhysRevLett.10.531.

[11] M. Kobayashi and T. Maskawa, "CP Violation in the Renormalizable Theory of Weak Interaction," *Prog. Theor. Phys.* **49** (1973) 652–657.

[12] E. Noether and M. A. Tavel, "Invariant variation problems," `arXiv:physics/0503066`.

[13] J. C. Ward, "An identity in quantum electrodynamics," *Phys. Rev.* **78** (Apr, 1950) 182–182. https://link.aps.org/doi/10.1103/PhysRev.78.182.

[14] Y. Takahashi, "On the generalized ward identity," *Il Nuovo Cimento (1955-1965)* **6** no. 2, (Aug, 1957) 371–375. https://doi.org/10.1007/BF02832514.

[15] G. 'tHooft, "Renormalization of massless yang-mills fields," *Nuclear Physics B* **33** no. 1, (1971) 173 – 199. http://www.sciencedirect.com/science/article/pii/0550321371903956.

[16] J. Taylor, "Ward identities and charge renormalization of the yang-mills field," *Nuclear Physics B* **33** no. 2, (1971) 436 – 444. http://www.sciencedirect.com/science/article/pii/0550321371902975.

[17] A. A. Slavnov, "Ward identities in gauge theories," *Theoretical and Mathematical Physics* **10** no. 2, (Feb, 1972) 99–104. https://doi.org/10.1007/BF01090719.

[18] C. N. Yang and R. L. Mills, "Conservation of isotopic spin and isotopic gauge invariance," *Phys. Rev.* **96** (Oct, 1954) 191–195. https://link.aps.org/doi/10.1103/PhysRev.96.191.

[19] K. G. Wilson, "Confinement of quarks," *Phys. Rev. D* **10** (Oct, 1974) 2445–2459. https://link.aps.org/doi/10.1103/PhysRevD.10.2445.

[20] T. DeGrand and C. DeTar, *Lattice Methods for Quantum Chromodynamics.* World Scientific, Singapore, 2006. https://cds.cern.ch/record/1055545.

[21] S. L. Glashow, "Partial-symmetries of weak interactions," *Nuclear Physics* **22** no. 4, (1961) 579 – 588. http://www.sciencedirect.com/science/article/pii/0029558261904692.

[22] S. Weinberg, "A model of leptons," *Phys. Rev. Lett.* **19** (Nov, 1967) 1264–1266. https://link.aps.org/doi/10.1103/PhysRevLett.19.1264.

[23] A. Salam and J. C. Ward, "Weak and electromagnetic interactions," *Il Nuovo Cimento (1955-1965)* **11** no. 4, (Feb, 1959) 568–577. https://doi.org/10.1007/BF02726525.

[24] C. S. Wu, E. Ambler, R. W. Hayward, D. D. Hoppes, and R. P. Hudson, "Experimental test of parity conservation in beta decay," *Phys. Rev.* **105** (Feb, 1957) 1413–1415. https://link.aps.org/doi/10.1103/PhysRev.105.1413.

[25] M. Gell-Mann, "The interpretation of the new particles as displaced charge multiplets," *Il Nuovo Cimento (1955-1965)* **4** no. 2, (Apr, 1956) 848–866. https://doi.org/10.1007/BF02748000.

[26] K. Nishijima, "Charge Independence Theory of V Particles*," *Progress of Theoretical Physics* **13** no. 3, (03, 1955) 285–304, https://academic.oup.com/ptp/article-pdf/13/3/285/5425869/13-3-285.pdf. https://doi.org/10.1143/PTP.13.285.

[27] T. Nakano and K. Nishijima, "Charge Independence for V-particles*," *Progress of Theoretical Physics* **10** no. 5, (11, 1953) 581–582, https://academic.oup.com/ptp/article-pdf/10/5/581/5364926/10-5-581.pdf. https://doi.org/10.1143/PTP.10.581.

[28] F. Englert and R. Brout, "Broken symmetry and the mass of gauge vector mesons," *Phys. Rev. Lett.* **13** (Aug, 1964) 321–323. https://link.aps.org/doi/10.1103/PhysRevLett.13.321.

[29] P. W. Higgs, "Broken symmetries and the masses of gauge bosons," *Phys. Rev. Lett.* **13** (Oct, 1964) 508–509. https://link.aps.org/doi/10.1103/PhysRevLett.13.508.

[30] P. W. Higgs, "Spontaneous symmetry breakdown without massless bosons," *Phys. Rev.* **145** (May, 1966) 1156–1163. https://link.aps.org/doi/10.1103/PhysRev.145.1156.

[31] Y. Nambu, "Quasiparticles and Gauge Invariance in the Theory of Superconductivity," *Phys. Rev.* **117** (1960) 648–663. [,132(1960)].

[32] J. Goldstone, "Field Theories with Superconductor Solutions," *Nuovo Cim.* **19** (1961) 154–164.

[33] V. Brdar, A. J. Helmboldt, S. Iwamoto, and K. Schmitz, "Type-I Seesaw as the Common Origin of Neutrino Mass, Baryon Asymmetry, and the Electroweak Scale," *Phys. Rev. D* **100** (2019) 075029, arXiv:1905.12634 [hep-ph].

[34] G. 't Hooft and M. Veltman, "Regularization and renormalization of gauge fields," *Nuclear Physics B* **44** no. 1, (1972) 189 – 213. http://www.sciencedirect.com/science/article/pii/0550321372902799.

[35] F. Zwicky, "Die Rotverschiebung von extragalaktischen Nebeln," *Helv. Phys. Acta* **6** (1933) 110–127. https://cds.cern.ch/record/437297.

[36] V. C. Rubin and W. K. Ford, Jr., "Rotation of the Andromeda Nebula from a Spectroscopic Survey of Emission Regions," *Astrophys. J.* **159** (1970) 379–403.

[37] G. Bertone, D. Hooper, and J. Silk, "Particle dark matter: Evidence, candidates and constraints," *Phys. Rept.* **405** (2005) 279–390, arXiv:hep-ph/0404175.

[38] D. Clowe, M. Bradac, A. H. Gonzalez, M. Markevitch, S. W. Randall, C. Jones, and D. Zaritsky, "A direct empirical proof of the existence of dark matter," *Astrophys. J.* **648** (2006) L109–L113, arXiv:astro-ph/0608407 [astro-ph].

[39] A. Taylor, S. Dye, T. J. Broadhurst, N. Benitez, and E. van Kampen, "Gravitational lens magnification and the mass of abell 1689," *Astrophys. J.* **501** (1998) 539, arXiv:astro-ph/9801158.

[40] C. Bennett *et al.*, "Four year COBE DMR cosmic microwave background observations: Maps and basic results," *Astrophys. J. Lett.* **464** (1996) L1–L4, arXiv:astro-ph/9601067.

[41] G. F. Smoot *et al.*, "Structure in the COBE Differential Microwave Radiometer First-Year Maps," *ApJS* **396** (September, 1992) L1.

[42] **WMAP** Collaboration, "Nine-year Wilkinson Microwave Anisotropy Probe (WMAP) Observations: Final Maps and Results," *ApJS* **208** no. 2, (October, 2013) 20, arXiv:1212.5225 [astro-ph.CO].

[43] **WMAP** Collaboration, "Nine-year Wilkinson Microwave Anisotropy Probe (WMAP) Observations: Cosmological Parameter Results," *ApJS* **208** no. 2, (October, 2013) 19, arXiv:1212.5226 [astro-ph.CO].

[44] **Planck** Collaboration, "Planck 2018 results. I. Overview and the cosmological legacy of Planck," *Astron. Astrophys.* **641** (2020) A1, arXiv:1807.06205 [astro-ph.CO].

[45] A. Liddle, *An introduction to modern cosmology; 3rd ed.* Wiley, Chichester, Mar, 2015. https://cds.cern.ch/record/1976476.

[46] **Planck** Collaboration, "Planck 2018 results. VI. Cosmological parameters," *Astron. Astrophys.* **641** (2020) A6, arXiv:1807.06209 [astro-ph.CO].

[47] H. Georgi and S. L. Glashow, "Unity of all elementary-particle forces," *Phys. Rev. Lett.* **32** (Feb, 1974) 438–441. https://link.aps.org/doi/10.1103/PhysRevLett.32.438.

[48] I. Aitchison, *Supersymmetry in Particle Physics. An Elementary Introduction.* Cambridge University Press, Cambridge, 2007.

[49] **Muon g-2** Collaboration, G. Bennett *et al.*, "Final Report of the Muon E821 Anomalous Magnetic Moment Measurement at BNL," *Phys. Rev. D* **73** (2006) 072003, `arXiv:hep-ex/0602035`.

[50] H. Baer and X. Tata, *Weak Scale Supersymmetry: From Superfields to Scattering Events.* Cambridge University Press, 2006.

[51] A. Czarnecki and W. J. Marciano, "The Muon anomalous magnetic moment: A Harbinger for 'new physics'," *Phys. Rev. D* **64** (2001) 013014, `arXiv:hep-ph/0102122`.

[52] J. L. Feng and K. T. Matchev, "Supersymmetry and the anomalous magnetic moment of the muon," *Phys. Rev. Lett.* **86** (2001) 3480–3483, `arXiv:hep-ph/0102146`.

[53] S. Coleman and J. Mandula, "All possible symmetries of the s matrix," *Phys. Rev.* **159** (Jul, 1967) 1251–1256. https://link.aps.org/doi/10.1103/PhysRev.159.1251.

[54] R. Haag, J. T. Lopuszanski, and M. Sohnius, "All Possible Generators of Supersymmetries of the s Matrix," *Nucl. Phys.* **B88** (1975) 257. [,257(1974)].

[55] J. Wess and B. Zumino, "Supergauge transformations in four dimensions," *Nuclear Physics B* **70** no. 1, (1974) 39 – 50. http://www.sciencedirect.com/science/article/pii/0550321374903551.

[56] H. Georgi and S. L. Glashow, "Gauge theories without anomalies," *Phys. Rev. D* **6** (Jul, 1972) 429–431. https://link.aps.org/doi/10.1103/PhysRevD.6.429.

[57] S. Dimopoulos and D. W. Sutter, "The Supersymmetric flavor problem," *Nucl. Phys. B* **452** (1995) 496–512, `arXiv:hep-ph/9504415`.

[58] **MEG** Collaboration, T. Mori, "Final Results of the MEG Experiment," *Nuovo Cim. C* **39** no. 4, (2017) 325, `arXiv:1606.08168 [hep-ex]`.

[59] H. P. Nilles, "Supersymmetry, Supergravity and Particle Physics," *Phys. Rept.* **110** (1984) 1–162.

[60] A. Lahanas and D. Nanopoulos, "The road to no-scale supergravity," *Physics Reports* **145** no. 1, (1987) 1 – 139. http://www.sciencedirect.com/science/article/pii/0370157387900342.

[61] J. L. Feng, A. Rajaraman, and F. Takayama, "Superweakly interacting massive particles," *Phys. Rev. Lett.* **91** (2003) 011302, `arXiv:hep-ph/0302215`.

[62] **Super-Kamiokande** Collaboration, K. Abe *et al.*, "Search for proton decay via $p \to e^+ \pi^0$ and $p \to \mu^+ \pi^0$ in 0.31 megaton-years exposure of the Super-Kamiokande water Cherenkov detector," *Phys. Rev.* **D95** no. 1, (2017) 012004, `arXiv:1610.03597 [hep-ex]`.

[63] J. R. Ellis, "Beyond the standard model for hill walkers," in *1998 European School of High-Energy Physics*, pp. 133–196. 8, 1998. `arXiv:hep-ph/9812235`.

[64] J. R. Ellis, J. Hagelin, D. V. Nanopoulos, K. A. Olive, and M. Srednicki, "Supersymmetric Relics from the Big Bang," *Nucl. Phys. B* **238** (1984) 453–476.

[65] D. O. Caldwell, R. M. Eisberg, D. M. Grumm, M. S. Witherell, B. Sadoulet, F. S. Goulding, and A. R. Smith, "Laboratory limits on galactic cold dark matter," *Phys. Rev. Lett.* **61** (Aug, 1988) 510–513. https://link.aps.org/doi/10.1103/PhysRevLett.61.510.

[66] M. Mori, M. M. Nojiri, K. S. Hirata, K. Kihara, Y. Oyama, A. Suzuki, K. Takahashi, M. Yamada, H. Takei, M. Koga, K. Miyano, H. Miyata, Y. Fukuda, T. Hayakawa, K. Inoue, T. Ishida, T. Kajita, Y. Koshio, M. Nakahata, K. Nakamura, A. Sakai, N. Sato, M. Shiozawa, J. Suzuki, Y. Suzuki, Y. Totsuka, M. Koshiba, K. Nishijima, T. Kajimura, T. Suda, A. T. Suzuki, T. Hara, Y. Nagashima, M. Takita, H. Yokoyama, A. Yoshimoto, K. Kaneyuki, Y. Takeuchi, T. Tanimori, S. Tasaka, and K. Nishikawa, "Search for neutralino dark matter heavier than the w boson at kamiokande," *Phys. Rev. D* **48** (Dec, 1993) 5505–5518. https://link.aps.org/doi/10.1103/PhysRevD.48.5505.

[67] **CDMS** Collaboration, D. S. Akerib *et al.*, "Exclusion limits on the WIMP-nucleon cross section from the first run of the Cryogenic Dark Matter Search in the Soudan Underground Laboratory," *Phys. Rev. D* **72** (2005) 052009, arXiv:astro-ph/0507190.

[68] A. Djouadi, J.-L. Kneur, and G. Moultaka, "SuSpect: A Fortran code for the supersymmetric and Higgs particle spectrum in the MSSM," *Comput. Phys. Commun.* **176** (2007) 426–455, arXiv:hep-ph/0211331.

[69] C. F. Berger, J. S. Gainer, J. L. Hewett, and T. G. Rizzo, "Supersymmetry without prejudice," *Journal of High Energy Physics* **2009** no. 02, (Feb, 2009) 023–023. http://dx.doi.org/10.1088/1126-6708/2009/02/023.

[70] J. Alwall, P. Schuster, and N. Toro, "Simplified Models for a First Characterization of New Physics at the LHC," *Phys. Rev.* **D79** (2009) 075020, arXiv:0810.3921 [hep-ph].

[71] **LHC New Physics Working Group** Collaboration, D. Alves, "Simplified Models for LHC New Physics Searches," *J. Phys.* **G39** (2012) 105005, arXiv:1105.2838 [hep-ph].

[72] D. S. Alves, E. Izaguirre, and J. G. Wacker, "Where the Sidewalk Ends: Jets and Missing Energy Search Strategies for the 7 TeV LHC," *JHEP* **10** (2011) 012, arXiv:1102.5338 [hep-ph].

[73] F. Ambrogi, S. Kraml, S. Kulkarni, U. Laa, A. Lessa, and W. Waltenberger, "On the coverage of the pMSSM by simplified model results," *Eur. Phys. J. C* **78** no. 3, (2018) 215, arXiv:1707.09036 [hep-ph].

[74] O. Buchmueller and J. Marrouche, "Universal mass limits on gluino and third-generation squarks in the context of Natural-like SUSY spectra," *Int. J. Mod. Phys. A* **29** no. 06, (2014) 1450032, arXiv:1304.2185 [hep-ph].

[75] **ATLAS** Collaboration, M. Aaboud *et al.*, "Dark matter interpretations of ATLAS searches for the electroweak production of supersymmetric particles in $\sqrt{s} = 8$ TeV proton-proton collisions," *JHEP* **09** (2016) 175, arXiv:1608.00872 [hep-ex].

[76] **ATLAS** Collaboration, "Summary of the ATLAS experiment's sensitivity to supersymmetry after LHC Run 1 — interpreted in the phenomenological MSSM," *JHEP* **10** (2015) 134, arXiv:1508.06608 [hep-ex].

[77] **ATLAS** Collaboration, "Mass reach of the atlas searches for supersymmetry." https://atlas.web.cern.ch/Atlas/GROUPS/PHYSICS/PUBNOTES/ATL-PHYS-PUB-2020-020/fig__23.png, 2020.

[78] **CMS** Collaboration, "Summary plot moriond 2017." https://twiki.cern.ch/twiki/pub/CMSPublic/SUSYSummary2017/Moriond2017__BarPlot.pdf, 2017.

[79] L. S. W. Group, "Notes lepsusywg/02-04.1 and lepsusywg/01-03.1." http://lepsusy.web.cern.ch/lepsusy/, 2004. Accessed: 2021-02-11.

[80] **ATLAS** Collaboration, G. Aad *et al.*, "Observation of a new particle in the search for the Standard Model Higgs boson with the ATLAS detector at the LHC," *Phys. Lett. B* **716** (2012) 1–29, `arXiv:1207.7214 [hep-ex]`.

[81] **CMS** Collaboration, S. Chatrchyan *et al.*, "Observation of a New Boson at a Mass of 125 GeV with the CMS Experiment at the LHC," *Phys. Lett. B* **716** (2012) 30–61, `arXiv:1207.7235 [hep-ex]`.

[82] CERN, "About cern." https://home.cern/about. Accessed: 2021-01-21.

[83] CERN, "CERN Annual report 2019," tech. rep., CERN, Geneva, 2020. https://cds.cern.ch/record/2723123.

[84] O. S. Bruning, P. Collier, P. Lebrun, S. Myers, R. Ostojic, J. Poole, and P. Proudlock, *LHC Design Report.* CERN Yellow Reports: Monographs. CERN, Geneva, 2004. https://cds.cern.ch/record/782076.

[85] M. Blewett and N. Vogt-Nilsen, "Proceedings of the 8th international conference on high-energy accelerators, cern 1971. conference held at geneva, 20–24 september 1971.," tech. rep., 1971, 1971.

[86] L. R. Evans and P. Bryant, "LHC Machine," *JINST* **3** (2008) S08001. 164 p. http://cds.cern.ch/record/1129806. This report is an abridged version of the LHC Design Report (CERN-2004-003).

[87] R. Scrivens, M. Kronberger, D. Küchler, J. Lettry, C. Mastrostefano, O. Midttun, M. O'Neil, H. Pereira, and C. Schmitzer, "Overview of the status and developments on primary ion sources at CERN*,". https://cds.cern.ch/record/1382102.

[88] M. Vretenar, J. Vollaire, R. Scrivens, C. Rossi, F. Roncarolo, S. Ramberger, U. Raich, B. Puccio, D. Nisbet, R. Mompo, S. Mathot, C. Martin, L. A. Lopez-Hernandez, A. Lombardi, J. Lettry, J. B. Lallement, I. Kozsar, J. Hansen, F. Gerigk, A. Funken, J. F. Fuchs, N. Dos Santos, M. Calviani, M. Buzio, O. Brunner, Y. Body, P. Baudrenghien, J. Bauche, and T. Zickler, *Linac4 design report*, vol. 6 of *CERN Yellow Reports: Monographs.* CERN, Geneva, 2020. https://cds.cern.ch/record/2736208.

[89] E. Mobs, "The CERN accelerator complex - 2019. Complexe des accélérateurs du CERN - 2019,". https://cds.cern.ch/record/2684277. General Photo.

[90] **ATLAS** Collaboration, "The ATLAS Experiment at the CERN Large Hadron Collider," *JINST* **3** (2008) S08003.

[91] **CMS** Collaboration, S. Chatrchyan *et al.*, "The CMS Experiment at the CERN LHC," *JINST* **3** (2008) S08004.

[92] **ALICE** Collaboration, K. Aamodt *et al.*, "The ALICE experiment at the CERN LHC," *JINST* **3** (2008) S08002.

[93] **LHCb** Collaboration, J. Alves, A.Augusto *et al.*, "The LHCb Detector at the LHC," *JINST* **3** (2008) S08005.

[94] **TOTEM** Collaboration, G. Anelli *et al.*, "The TOTEM experiment at the CERN Large Hadron Collider," *JINST* **3** (2008) S08007.

[95] **LHCf** Collaboration, O. Adriani *et al.*, "Technical design report of the LHCf experiment: Measurement of photons and neutral pions in the very forward region of LHC,".

[96] **MoEDAL** Collaboration, J. Pinfold *et al.*, "Technical Design Report of the MoEDAL Experiment,".

[97] **ATLAS** Collaboration, "ATLAS Public Results - Luminosity Public Results Run 2,". https://twiki.cern.ch/twiki/bin/view/AtlasPublic/LuminosityPublicResultsRun2. Accessed: 2021-01-17.

[98] **ATLAS** Collaboration, Z. Marshall, "Simulation of Pile-up in the ATLAS Experiment," *J. Phys. Conf. Ser.* **513** (2014) 022024.

[99] "First beam in the LHC - accelerating science,". https://home.cern/news/news/accelerators/record-luminosity-well-done-lhc. Accessed: 2021-01-10.

[100] **ATLAS Collaboration** Collaboration, "Luminosity determination in *pp* collisions at $\sqrt{s} = 13$ TeV using the ATLAS detector at the LHC," Tech. Rep. ATLAS-CONF-2019-021, CERN, Geneva, Jun, 2019. https://cds.cern.ch/record/2677054.

[101] **ATLAS** Collaboration, M. Aaboud *et al.*, "Luminosity determination in pp collisions at $\sqrt{s} = 8$ TeV using the ATLAS detector at the LHC," *Eur. Phys. J. C* **76** no. 12, (2016) 653, arXiv:1608.03953 [hep-ex].

[102] G. Avoni, M. Bruschi, G. Cabras, D. Caforio, N. Dehghanian, A. Floderus, B. Giacobbe, F. Giannuzzi, F. Giorgi, P. Grafström, V. Hedberg, F. L. Manghi, S. Meneghini, J. Pinfold, E. Richards, C. Sbarra, N. S. Cesari, A. Sbrizzi, R. Soluk, G. Ucchielli, S. Valentinetti, O. Viazlo, M. Villa, C. Vittori, R. Vuillermet, and A. Zoccoli, "The new LUCID-2 detector for luminosity measurement and monitoring in ATLAS," *Journal of Instrumentation* **13** no. 07, (Jul, 2018) P07017–P07017. https://doi.org/10.1088/1748-0221/13/07/p07017.

[103] S. van der Meer, "Calibration of the effective beam height in the ISR," Tech. Rep. CERN-ISR-PO-68-31. ISR-PO-68-31, CERN, Geneva, 1968. https://cds.cern.ch/record/296752.

[104] P. Grafström and W. Kozanecki, "Luminosity determination at proton colliders," *Progress in Particle and Nuclear Physics* **81** (2015) 97 – 148. http://www.sciencedirect.com/science/article/pii/S0146641014000878.

[105] "New schedule for CERN's accelerators and experiments,". https://home.cern/news/press-release/cern/first-beam-lhc-accelerating-science. Accessed: 2021-01-10.

[106] **ATLAS** Collaboration, G. Aad *et al.*, "Luminosity Determination in *pp* Collisions at $\sqrt{s} = 7$ TeV Using the ATLAS Detector at the LHC," *Eur. Phys. J. C* **71** (2011) 1630, `arXiv:1101.2185 [hep-ex]`.

[107] **ATLAS Collaboration** Collaboration, G. Aad *et al.*, "Improved luminosity determination in pp collisions at $\sqrt{s} = 7$ TeV using the ATLAS detector at the LHC. Improved luminosity determination in pp collisions at sqrt(s) = 7 TeV using the ATLAS detector at the LHC," *Eur. Phys. J. C* **73** no. CERN-PH-EP-2013-026. CERN-PH-EP-2013-026, (Feb, 2013) 2518. 27 p. https://cds.cern.ch/record/1517411. Comments: 26 pages plus author list (39 pages total), 17 figures, 9 tables, submitted to EPJC, All figures are available at <a href=.

[108] "Record luminosity: well done LHC,". https://home.cern/news/news/accelerators/new-schedule-cerns-accelerators-and-experiments. Accessed: 2021-01-10.

[109] A. G., B. A. I., B. O., F. P., L. M., R. L., and T. L., *High-Luminosity Large Hadron Collider (HL-LHC): Technical Design Report V. 0.1*. CERN Yellow Reports: Monographs. CERN, Geneva, 2017. https://cds.cern.ch/record/2284929.

[110] J. Pequenao, "Computer generated image of the whole ATLAS detector." Mar, 2008.

[111] **ATLAS** Collaboration, "ATLAS: Detector and physics performance technical design report. Volume 1,".

[112] J. Pequenao, "Computer generated image of the ATLAS inner detector." Mar, 2008.

[113] **ATLAS Collaboration** Collaboration, K. Potamianos, "The upgraded Pixel detector and the commissioning of the Inner Detector tracking of the ATLAS experiment for Run-2 at the Large Hadron Collider," Tech. Rep. ATL-PHYS-PROC-2016-104, CERN, Geneva, Aug, 2016. https://cds.cern.ch/record/2209070. 15 pages, EPS-HEP 2015 Proceedings.

[114] **ATLAS IBL** Collaboration, B. Abbott *et al.*, "Production and Integration of the ATLAS Insertable B-Layer," *JINST* **13** no. 05, (2018) T05008, `arXiv:1803.00844 [physics.ins-det]`.

[115] **ATLAS** Collaboration, "ATLAS Insertable B-Layer Technical Design Report," Tech. Rep. CERN-LHCC-2010-013. ATLAS-TDR-19, Sep, 2010. http://cds.cern.ch/record/1291633.

[116] **ATLAS** Collaboration, G. Aad *et al.*, "ATLAS b-jet identification performance and efficiency measurement with $t\bar{t}$ events in pp collisions at $\sqrt{s} = 13$ TeV," *Eur. Phys. J. C* **79** no. 11, (2019) 970, `arXiv:1907.05120 [hep-ex]`.

[117] ATLAS Collaboration, "Particle Identification Performance of the ATLAS Transition Radiation Tracker." ATLAS-CONF-2011-128, 2011. https://cds.cern.ch/record/1383793.

[118] J. Pequenao, "Computer Generated image of the ATLAS calorimeter." Mar, 2008.

[119] J. Pequenao, "Computer generated image of the ATLAS Muons subsystem." Mar, 2008.

[120] S. Lee, M. Livan, and R. Wigmans, "Dual-Readout Calorimetry," *Rev. Mod. Phys.* **90** no. arXiv:1712.05494. 2, (Dec, 2017) 025002. 40 p. https://cds.cern.ch/record/2637852. 44 pages, 53 figures, accepted for publication in Review of Modern Physics.

[121] M. Leite, "Performance of the ATLAS Zero Degree Calorimeter," Tech. Rep. ATL-FWD-PROC-2013-001, CERN, Geneva, Nov, 2013. https://cds.cern.ch/record/1628749.

[122] S. Abdel Khalek *et al.*, "The ALFA Roman Pot Detectors of ATLAS," *JINST* **11** no. 11, (2016) P11013, `arXiv:1609.00249 [physics.ins-det]`.

[123] U. Amaldi, G. Cocconi, A. Diddens, R. Dobinson, J. Dorenbosch, W. Duinker, D. Gustavson, J. Meyer, K. Potter, A. Wetherell, A. Baroncelli, and C. Bosio, "The real part of the forward proton proton scattering amplitude measured at the cern intersecting storage rings," *Physics Letters B* **66** no. 4, (1977) 390 – 394. http://www.sciencedirect.com/science/article/pii/0370269377900223.

[124] L. Adamczyk, E. Banaś, A. Brandt, M. Bruschi, S. Grinstein, J. Lange, M. Rijssenbeek, P. Sicho, R. Staszewski, T. Sykora, M. Trzebiński, J. Chwastowski, and K. Korcyl, "Technical Design Report for the ATLAS Forward Proton Detector," Tech. Rep. CERN-LHCC-2015-009. ATLAS-TDR-024, May, 2015. https://cds.cern.ch/record/2017378.

[125] **ATLAS** Collaboration, A. R. Martínez, "The Run-2 ATLAS Trigger System," *J. Phys. Conf. Ser.* **762** no. 1, (2016) 012003.

[126] **ATLAS Collaboration** Collaboration, *ATLAS level-1 trigger: Technical Design Report.* Technical Design Report ATLAS. CERN, Geneva, 1998. https://cds.cern.ch/record/381429.

[127] **ATLAS** Collaboration, G. Aad *et al.*, "Operation of the ATLAS trigger system in Run 2," *JINST* **15** no. 10, (2020) P10004, `arXiv:2007.12539 [physics.ins-det]`.

[128] **ATLAS Collaboration** Collaboration, P. Jenni, M. Nessi, M. Nordberg, and K. Smith, *ATLAS high-level trigger, data-acquisition and controls: Technical Design Report.* Technical Design Report ATLAS. CERN, Geneva, 2003. https://cds.cern.ch/record/616089.

[129] **ATLAS** Collaboration, G. Aad *et al.*, "The ATLAS Simulation Infrastructure," *Eur. Phys. J. C* **70** (2010) 823–874, `arXiv:1005.4568 [physics.ins-det]`.

[130] T. Gleisberg, S. Hoeche, F. Krauss, M. Schonherr, S. Schumann, F. Siegert, and J. Winter, "Event generation with SHERPA 1.1," *JHEP* **02** (2009) 007, `arXiv:0811.4622 [hep-ph]`.

[131] A. Buckley *et al.*, "General-purpose event generators for LHC physics," *Phys. Rept.* **504** (2011) 145–233, `arXiv:1101.2599 [hep-ph]`.

[132] V. N. Gribov and L. N. Lipatov, "Deep inelastic e p scattering in perturbation theory," *Sov. J. Nucl. Phys.* **15** (1972) 438–450.

[133] J. Blumlein, T. Doyle, F. Hautmann, M. Klein, and A. Vogt, "Structure functions in deep inelastic scattering at HERA," in *Workshop on Future Physics at HERA (To be followed by meetings 7-9 Feb and 30-31 May 1996 at DESY).* 9, 1996. `arXiv:hep-ph/9609425`.

[134] A. Buckley, J. Ferrando, S. Lloyd, K. Nordström, B. Page, M. Rüfenacht, M. Schönherr, and G. Watt, "LHAPDF6: parton density access in the LHC precision era," *Eur. Phys. J. C* **75** (2015) 132, `arXiv:1412.7420 [hep-ph]`.

[135] M. Bengtsson and T. Sjostrand, "Coherent Parton Showers Versus Matrix Elements: Implications of PETRA - PEP Data," *Phys. Lett. B* **185** (1987) 435.

[136] S. Catani, F. Krauss, R. Kuhn, and B. R. Webber, "QCD matrix elements + parton showers," *JHEP* **11** (2001) 063, `arXiv:hep-ph/0109231`.

[137] L. Lonnblad, "Correcting the color dipole cascade model with fixed order matrix elements," *JHEP* **05** (2002) 046, `arXiv:hep-ph/0112284`.

[138] B. Andersson, G. Gustafson, G. Ingelman, and T. Sjostrand, "Parton Fragmentation and String Dynamics," *Phys. Rept.* **97** (1983) 31–145.

[139] B. Andersson, *The Lund Model*. Cambridge Monographs on Particle Physics, Nuclear Physics and Cosmology. Cambridge University Press, 1998.

[140] D. Amati and G. Veneziano, "Preconfinement as a Property of Perturbative QCD," *Phys. Lett. B* **83** (1979) 87–92.

[141] D. Yennie, S. Frautschi, and H. Suura, "The infrared divergence phenomena and high-energy processes," *Annals of Physics* **13** no. 3, (1961) 379–452. https://www.sciencedirect.com/science/article/pii/0003491661901518.

[142] M. Dobbs and J. B. Hansen, "The HepMC C++ Monte Carlo event record for High Energy Physics," *Comput. Phys. Commun.* **134** (2001) 41–46.

[143] **GEANT4** Collaboration, S. Agostinelli *et al.*, "GEANT4: A Simulation toolkit," *Nucl. Instrum. Meth.* **A506** (2003) 250–303.

[144] **ATLAS Collaboration** Collaboration, "The new Fast Calorimeter Simulation in ATLAS," Tech. Rep. ATL-SOFT-PUB-2018-002, CERN, Geneva, Jul, 2018. https://cds.cern.ch/record/2630434.

[145] K. Cranmer, "Practical Statistics for the LHC," in *2011 European School of High-Energy Physics*, pp. 267–308. 2014. `arXiv:1503.07622 [physics.data-an]`.

[146] G. Cowan, K. Cranmer, E. Gross, and O. Vitells, "Asymptotic formulae for likelihood-based tests of new physics," *Eur. Phys. J.* **C71** (2011) 1554, `arXiv:1007.1727 [physics.data-an]`. [Erratum: Eur. Phys. J.C73,2501(2013)].

[147] ATLAS Collaboration, "Reproduction searches for new physics with the ATLAS experiment through publication of full statistical likelihoods." ATL-PHYS-PUB-2019-029, 2019. https://cds.cern.ch/record/2684863.

[148] **ROOT Collaboration** Collaboration, K. Cranmer, G. Lewis, L. Moneta, A. Shibata, and W. Verkerke, "HistFactory: A tool for creating statistical models for use with RooFit and RooStats," Tech. Rep. CERN-OPEN-2012-016, New York U., New York, Jan, 2012. https://cds.cern.ch/record/1456844.

[149] W. Verkerke and D. P. Kirkby, "The RooFit toolkit for data modeling," *eConf* **C0303241** (2003) MOLT007, `arXiv:physics/0306116 [physics]`. [,186(2003)].

[150] L. Moneta, K. Belasco, K. S. Cranmer, S. Kreiss, A. Lazzaro, D. Piparo, G. Schott, W. Verkerke, and M. Wolf, "The RooStats Project," *PoS* **ACAT2010** (2010) 057, `arXiv:1009.1003 [physics.data-an]`.

[151] F. James and M. Roos, "MINUIT: a system for function minimization and analysis of the parameter errors and corrections," *Comput. Phys. Commun.* **10** no. CERN-DD-75-20, (Jul, 1975) 343–367. 38 p. https://cds.cern.ch/record/310399.

[152] R. Brun and F. Rademakers, "ROOT: An object oriented data analysis framework," *Nucl. Instrum. Meth.* **A389** (1997) 81–86.

[153] I. Antcheva *et al.*, "Root — a c++ framework for petabyte data storage, statistical analysis and visualization," *Computer Physics Communications* **182** no. 6, (2011) 1384 – 1385. http://www.sciencedirect.com/science/article/pii/S0010465511000701.

[154] M. Baak, G. J. Besjes, D. Côte, A. Koutsman, J. Lorenz, and D. Short, "HistFitter software framework for statistical data analysis," *Eur. Phys. J.* **C75** (2015) 153, arXiv:1410.1280 [hep-ex].

[155] L. Heinrich, M. Feickert, G. Stark, and K. Cranmer, "pyhf: pure-python implementation of histfactory statistical models," *Journal of Open Source Software* **6** no. 58, (2021) 2823. https://doi.org/10.21105/joss.02823.

[156] L. Heinrich, M. Feickert, and G. Stark, "pyhf: v0.6.0." https://github.com/scikit-hep/pyhf.

[157] C. R. Harris, K. J. Millman, S. J. van der Walt, R. Gommers, P. Virtanen, D. Cournapeau, E. Wieser, J. Taylor, S. Berg, N. J. Smith, R. Kern, M. Picus, S. Hoyer, M. H. van Kerkwijk, M. Brett, A. Haldane, J. F. del R'ıo, M. Wiebe, P. Peterson, P. G'erard-Marchant, K. Sheppard, T. Reddy, W. Weckesser, H. Abbasi, C. Gohlke, and T. E. Oliphant, "Array programming with NumPy," *Nature* **585** no. 7825, (Sept., 2020) 357–362. https://doi.org/10.1038/s41586-020-2649-2.

[158] A. Paszke, S. Gross, F. Massa, A. Lerer, J. Bradbury, G. Chanan, T. Killeen, Z. Lin, N. Gimelshein, L. Antiga, A. Desmaison, A. Kopf, E. Yang, Z. DeVito, M. Raison, A. Tejani, S. Chilamkurthy, B. Steiner, L. Fang, J. Bai, and S. Chintala, "Pytorch: An imperative style, high-performance deep learning library," in *Advances in Neural Information Processing Systems 32*, H. Wallach, H. Larochelle, A. Beygelzimer, F. d'Alché-Buc, E. Fox, and R. Garnett, eds., pp. 8024–8035. Curran Associates, Inc., 2019. http://papers.neurips.cc/paper/9015-pytorch-an-imperative-style-high-performance-deep-learning-library.pdf.

[159] M. Abadi, A. Agarwal, P. Barham, E. Brevdo, Z. Chen, C. Citro, G. S. Corrado, A. Davis, J. Dean, M. Devin, S. Ghemawat, I. Goodfellow, A. Harp, G. Irving, M. Isard, Y. Jia, R. Jozefowicz, L. Kaiser, M. Kudlur, J. Levenberg, D. Mané, R. Monga, S. Moore, D. Murray, C. Olah, M. Schuster, J. Shlens, B. Steiner, I. Sutskever, K. Talwar, P. Tucker, V. Vanhoucke, V. Vasudevan, F. Viégas, O. Vinyals, P. Warden, M. Wattenberg, M. Wicke, Y. Yu, and X. Zheng, "TensorFlow: Large-scale machine learning on heterogeneous systems," 2015. https://www.tensorflow.org/. Software available from tensorflow.org.

[160] J. Bradbury, R. Frostig, P. Hawkins, M. J. Johnson, C. Leary, D. Maclaurin, and S. Wanderman-Milne, "JAX: composable transformations of Python+NumPy programs," 2018. http://github.com/google/jax.

[161] S. S. Wilks, "The large-sample distribution of the likelihood ratio for testing composite hypotheses," *Ann. Math. Statist.* **9** no. 1, (03, 1938) 60–62. https://doi.org/10.1214/aoms/1177732360.

[162] A. Wald, "Tests of statistical hypotheses concerning several parameters when the number of observations is large," *Transactions of the American Mathematical Society* **54** no. 3, (1943) 426–482. https://doi.org/10.1090/S0002-9947-1943-0012401-3.

[163] G. Cowan, "Statistics for Searches at the LHC," in *69th Scottish Universities Summer School in Physics: LHC Physics*, pp. 321–355. 7, 2013. arXiv:1307.2487 [hep-ex].

[164] A. L. Read, "Presentation of search results: the CL_S technique," *J. Phys. G* **28** (2002) 2693.

[165] R. D. Cousins, J. T. Linnemann, and J. Tucker, "Evaluation of three methods for calculating statistical significance when incorporating a systematic uncertainty into a test of the background-only hypothesis for a Poisson process," *Nucl. Instrum. Meth. A* **595** no. 2, (2008) 480, arXiv:physics/0702156 [physics.data-an].

[166] K. CRANMER, "Statistical challenges for searches for new physics at the lhc," *Statistical Problems in Particle Physics, Astrophysics and Cosmology* (May, 2006) . http://dx.doi.org/10.1142/9781860948985_0026.

[167] ATLAS Collaboration, "Search for direct pair production of a chargino and a neutralino decaying to the 125 GeV Higgs boson in $\sqrt{s} = 8$ TeV pp collisions with the ATLAS detector," *Eur. Phys. J. C* **75** (2015) 208, arXiv:1501.07110 [hep-ex].

[168] ATLAS Collaboration, "Search for chargino and neutralino production in final states with a Higgs boson and missing transverse momentum at $\sqrt{s} = 13$ TeV with the ATLAS detector," *Phys. Rev. D* **100** (2019) 012006, arXiv:1812.09432 [hep-ex].

[169] CMS Collaboration, "Search for electroweak production of charginos and neutralinos in WH events in proton–proton collisions at $\sqrt{s} = 13$ TeV," *JHEP* **11** (2017) 029, arXiv:1706.09933 [hep-ex].

[170] ATLAS Collaboration, "Search for direct production of electroweakinos in final states with one lepton, missing transverse momentum and a Higgs boson decaying into two b-jets in pp collisions at $\sqrt{s} = 13$ TeV with the ATLAS detector," *Eur. Phys. J. C* **80** (2020) 691, arXiv:1909.09226 [hep-ex].

[171] ATLAS Collaboration, "Improvements in $t\bar{t}$ modelling using NLO+PS Monte Carlo generators for Run 2." ATL-PHYS-PUB-2018-009, 2018. https://cds.cern.ch/record/2630327.

[172] ATLAS Collaboration, "Modelling of the $t\bar{t}H$ and $t\bar{t}V(V = W, Z)$ processes for $\sqrt{s} = 13$ TeV ATLAS analyses." ATL-PHYS-PUB-2016-005, 2016. https://cds.cern.ch/record/2120826.

[173] ATLAS Collaboration, "ATLAS simulation of boson plus jets processes in Run 2." ATL-PHYS-PUB-2017-006, 2017. https://cds.cern.ch/record/2261937.

[174] ATLAS Collaboration, "Multi-Boson Simulation for 13 TeV ATLAS Analyses." ATL-PHYS-PUB-2017-005, 2017. https://cds.cern.ch/record/2261933.

[175] J. Alwall, R. Frederix, S. Frixione, V. Hirschi, F. Maltoni, O. Mattelaer, H. S. Shao, T. Stelzer, P. Torrielli, and M. Zaro, "The automated computation of tree-level and next-to-leading order differential cross sections, and their matching to parton shower simulations," *JHEP* **07** (2014) 079, arXiv:1405.0301 [hep-ph].

[176] R. Frederix and S. Frixione, "Merging meets matching in MC@NLO," *JHEP* **12** (2012) 061, `arXiv:1209.6215 [hep-ph]`.

[177] T. Sjöstrand, S. Ask, J. R. Christiansen, R. Corke, N. Desai, P. Ilten, S. Mrenna, S. Prestel, C. O. Rasmussen, and P. Z. Skands, "An Introduction to PYTHIA 8.2," *Comput. Phys. Commun.* **191** (2015) 159–177, `arXiv:1410.3012 [hep-ph]`.

[178] L. Lönnblad and S. Prestel, "Matching tree-level matrix elements with interleaved showers," *JHEP* **03** (2012) 019, `arXiv:1109.4829 [hep-ph]`.

[179] R. D. Ball *et al.*, "Parton distributions with LHC data," *Nucl. Phys. B* **867** (2013) 244, `arXiv:1207.1303 [hep-ph]`.

[180] ATLAS Collaboration, "ATLAS Pythia 8 tunes to 7 TeV data." ATL-PHYS-PUB-2014-021, 2014. https://cds.cern.ch/record/1966419.

[181] D. J. Lange, "The EvtGen particle decay simulation package," *Nucl. Instrum. Meth. A* **462** (2001) 152.

[182] ATLAS Collaboration, "The Pythia 8 A3 tune description of ATLAS minimum bias and inelastic measurements incorporating the Donnachie–Landshoff diffractive model." ATL-PHYS-PUB-2016-017, 2016. https://cds.cern.ch/record/2206965.

[183] B. Fuks, M. Klasen, D. R. Lamprea, and M. Rothering, "Precision predictions for electroweak superpartner production at hadron colliders with RESUMMINO," *Eur. Phys. J. C* **73** (2013) 2480, `arXiv:1304.0790 [hep-ph]`.

[184] J. Fiaschi and M. Klasen, "Neutralino-chargino pair production at NLO+NLL with resummation-improved parton density functions for LHC Run II," *Phys. Rev. D* **98** no. 5, (2018) 055014, `arXiv:1805.11322 [hep-ph]`.

[185] B. Fuks, M. Klasen, D. R. Lamprea, and M. Rothering, "Gaugino production in proton-proton collisions at a center-of-mass energy of 8 TeV," *JHEP* **10** (2012) 081, `arXiv:1207.2159 [hep-ph]`.

[186] S. Alioli, P. Nason, C. Oleari, and E. Re, "A general framework for implementing NLO calculations in shower Monte Carlo programs: the POWHEG BOX," *JHEP* **06** (2010) 043, `arXiv:1002.2581 [hep-ph]`.

[187] S. Frixione, P. Nason, and G. Ridolfi, "A Positive-weight next-to-leading-order Monte Carlo for heavy flavour hadroproduction," *JHEP* **09** (2007) 126, `arXiv:0707.3088 [hep-ph]`.

[188] P. Nason, "A New method for combining NLO QCD with shower Monte Carlo algorithms," *JHEP* **11** (2004) 040, `arXiv:hep-ph/0409146`.

[189] E. Bothmann *et al.*, "Event generation with Sherpa 2.2," *SciPost Phys.* **7** no. 3, (2019) 034, `arXiv:1905.09127 [hep-ph]`.

[190] S. Höche, F. Krauss, S. Schumann, and F. Siegert, "QCD matrix elements and truncated showers," *JHEP* **05** (2009) 053, `arXiv:0903.1219 [hep-ph]`.

[191] S. Höche, F. Krauss, M. Schönherr, and F. Siegert, "QCD matrix elements + parton showers. The NLO case," *JHEP* **04** (2013) 027, `arXiv:1207.5030 [hep-ph]`.

[192] **NNPDF** Collaboration, R. D. Ball *et al.*, "Parton distributions for the LHC run II," *JHEP* **04** (2015) 040, `arXiv:1410.8849 [hep-ph]`.

[193] ATLAS Collaboration, "Example ATLAS tunes of Pythia8, Pythia6 and Powheg to an observable sensitive to Z boson transverse momentum." ATL-PHYS-PUB-2013-017, 2013. https://cds.cern.ch/record/1629317.

[194] M. Czakon and A. Mitov, "Top++: A program for the calculation of the top-pair cross-section at hadron colliders," *Comput. Phys. Commun.* **185** (2014) 2930, arXiv:1112.5675 [hep-ph].

[195] M. Cacciari, M. Czakon, M. Mangano, A. Mitov, and P. Nason, "Top-pair production at hadron colliders with next-to-next-to-leading logarithmic soft-gluon resummation," *Phys. Lett. B* **710** (2012) 612–622, arXiv:1111.5869 [hep-ph].

[196] P. Kant, O. M. Kind, T. Kintscher, T. Lohse, T. Martini, S. Mölbitz, P. Rieck, and P. Uwer, "HatHor for single top-quark production: Updated predictions and uncertainty estimates for single top-quark production in hadronic collisions," *Comput. Phys. Commun.* **191** (2015) 74–89, arXiv:1406.4403 [hep-ph].

[197] N. Kidonakis, "Two-loop soft anomalous dimensions for single top quark associated production with a W^- or H^-," *Phys. Rev. D* **82** (2010) 054018, arXiv:1005.4451 [hep-ph].

[198] J. M. Campbell and R. K. Ellis, "$t\bar{t}W^{+-}$ production and decay at NLO," *JHEP* **07** (2012) 052, arXiv:1204.5678 [hep-ph].

[199] A. Lazopoulos, T. McElmurry, K. Melnikov, and F. Petriello, "Next-to-leading order QCD corrections to $t\bar{t}Z$ production at the LHC," *Phys. Lett. B* **666** (2008) 62–65, arXiv:0804.2220 [hep-ph].

[200] R. Gavin, Y. Li, F. Petriello, and S. Quackenbush, "FEWZ 2.0: A code for hadronic Z production at next-to-next-to-leading order," arXiv:1011.3540 [hep-ph].

[201] **LHC Higgs Cross Section Working Group** Collaboration, D. de Florian *et al.*, "Handbook of LHC Higgs Cross Sections: 4. Deciphering the Nature of the Higgs Sector," arXiv:1610.07922 [hep-ph].

[202] ATLAS Collaboration, "Performance of the ATLAS track reconstruction algorithms in dense environments in LHC Run 2," *Eur. Phys. J. C* **77** (2017) 673, arXiv:1704.07983 [hep-ex].

[203] R. Frühwirth, "Application of Kalman filtering to track and vertex fitting," *Nucl. Instrum. Methods Phys. Res., A* **262** no. HEPHY-PUB-503, (Jun, 1987) 444. 19 p. https://cds.cern.ch/record/178627.

[204] T. Cornelissen, M. Elsing, I. Gavrilenko, W. Liebig, E. Moyse, and A. Salzburger, "The new ATLAS track reconstruction (NEWT)," *J. Phys.: Conf. Ser.* **119** (2008) 032014. https://cds.cern.ch/record/1176900.

[205] ATLAS Collaboration, "Vertex Reconstruction Performance of the ATLAS Detector at $\sqrt{s} = 13$ TeV." ATL-PHYS-PUB-2015-026, 2015. https://cds.cern.ch/record/2037717.

[206] ATLAS Collaboration, "Reconstruction of primary vertices at the ATLAS experiment in Run 1 proton–proton collisions at the LHC," *Eur. Phys. J. C* **77** (2017) 332, arXiv:1611.10235 [hep-ex].

[207] ATLAS Collaboration, "Topological cell clustering in the ATLAS calorimeters and its performance in LHC Run 1," *Eur. Phys. J. C* **77** (2017) 490, `arXiv:1603.02934 [hep-ex]`.

[208] ATLAS Collaboration, "Electron and photon performance measurements with the ATLAS detector using the 2015–2017 LHC proton–proton collision data," *JINST* **14** (2019) P12006, `arXiv:1908.00005 [hep-ex]`.

[209] ATLAS Collaboration, "Measurement of the photon identification efficiencies with the ATLAS detector using LHC Run 2 data collected in 2015 and 2016," *Eur. Phys. J. C* **79** (2019) 205, `arXiv:1810.05087 [hep-ex]`.

[210] ATLAS Collaboration, "Electron reconstruction and identification in the ATLAS experiment using the 2015 and 2016 LHC proton–proton collision data at $\sqrt{s} = 13$ TeV," *Eur. Phys. J. C* **79** (2019) 639, `arXiv:1902.04655 [hep-ex]`.

[211] ATLAS Collaboration, "Muon reconstruction performance of the ATLAS detector in proton–proton collision data at $\sqrt{s} = 13$ TeV," *Eur. Phys. J. C* **76** (2016) 292, `arXiv:1603.05598 [hep-ex]`.

[212] **ATLAS** Collaboration, "Muon reconstruction and identification efficiency in ATLAS using the full Run 2 pp collision data set at $\sqrt{s} = 13$ TeV," `arXiv:2012.00578 [hep-ex]`.

[213] M. Cacciari, G. P. Salam, and G. Soyez, "The anti-k_t jet clustering algorithm," *JHEP* **04** (2008) 063, `arXiv:0802.1189 [hep-ph]`.

[214] M. Cacciari, G. P. Salam, and G. Soyez, "FastJet user manual," *Eur. Phys. J. C* **72** (2012) 1896, `arXiv:1111.6097 [hep-ph]`.

[215] M. Cacciari, "FastJet: A Code for fast k_t clustering, and more," in *Deep inelastic scattering. Proceedings, 14th International Workshop, DIS 2006, Tsukuba, Japan, April 20-24, 2006*, pp. 487–490. 2006. `arXiv:hep-ph/0607071 [hep-ph]`. [,125(2006)].

[216] **ATLAS** Collaboration, G. Aad *et al.*, "Jet energy scale and resolution measured in proton-proton collisions at $\sqrt{s} = 13$ TeV with the ATLAS detector," `arXiv:2007.02645 [hep-ex]`.

[217] M. Cacciari and G. P. Salam, "Pileup subtraction using jet areas," *Phys. Lett. B* **659** (2008) 119–126, `arXiv:0707.1378 [hep-ph]`.

[218] ATLAS Collaboration, "Jet energy measurement with the ATLAS detector in proton–proton collisions at $\sqrt{s} = 7$ TeV," *Eur. Phys. J. C* **73** (2013) 2304, `arXiv:1112.6426 [hep-ex]`.

[219] ATLAS Collaboration, "Determination of jet calibration and energy resolution in proton–proton collisions at $\sqrt{s} = 8$ TeV using the ATLAS detector," `arXiv:1910.04482 [hep-ex]`.

[220] ATLAS Collaboration, "Performance of pile-up mitigation techniques for jets in pp collisions at $\sqrt{s} = 8$ TeV using the ATLAS detector," *Eur. Phys. J. C* **76** (2016) 581, `arXiv:1510.03823 [hep-ex]`.

[221] ATLAS Collaboration, "Optimisation and performance studies of the ATLAS b-tagging algorithms for the 2017-18 LHC run." ATL-PHYS-PUB-2017-013, 2017. https://cds.cern.ch/record/2273281.

[222] ATLAS Collaboration, "ATLAS b-jet identification performance and efficiency measurement with $t\bar{t}$ events in pp collisions at $\sqrt{s} = 13$ TeV," *Eur. Phys. J. C* **79** (2019) 970, arXiv:1907.05120 [hep-ex].

[223] ATLAS Collaboration, "Measurements of b-jet tagging efficiency with the ATLAS detector using $t\bar{t}$ events at $\sqrt{s} = 13$ TeV," *JHEP* **08** (2018) 089, arXiv:1805.01845 [hep-ex].

[224] ATLAS Collaboration, "Performance of missing transverse momentum reconstruction with the ATLAS detector using proton–proton collisions at $\sqrt{s} = 13$ TeV," *Eur. Phys. J. C* **78** (2018) 903, arXiv:1802.08168 [hep-ex].

[225] **ATLAS Collaboration** Collaboration, "$E_{\mathrm{T}}^{\mathrm{miss}}$ performance in the ATLAS detector using 2015-2016 LHC p-p collisions," Tech. Rep. ATLAS-CONF-2018-023, CERN, Geneva, Jun, 2018. http://cds.cern.ch/record/2625233.

[226] D. Adams *et al.*, "Recommendations of the Physics Objects and Analysis Harmonisation Study Groups 2014," Tech. Rep. ATL-PHYS-INT-2014-018, CERN, Geneva, Jul, 2014. https://cds.cern.ch/record/1743654.

[227] M. Cacciari, G. P. Salam, and G. Soyez, "The Catchment Area of Jets," *JHEP* **04** (2008) 005, arXiv:0802.1188 [hep-ph].

[228] **UA1** Collaboration, G. Arnison *et al.*, "Experimental Observation of Isolated Large Transverse Energy Electrons with Associated Missing Energy at $\sqrt{s} = 540$ GeV," *Phys. Lett. B* **122** (1983) 103–116.

[229] **Aachen-Annecy-Birmingham-CERN-Helsinki-London(QMC)-Paris(CdF)-Riverside-Rome-Rutherford-Saclay(CEN)-Vienna** Collaboration, G. Arnison *et al.*, "Further evidence for charged intermediate vector bosons at the SPS collider," *Phys. Lett. B* **129** no. CERN-EP-83-111, (Jun, 1985) 273–282. 17 p. https://cds.cern.ch/record/163856.

[230] D. R. Tovey, "On measuring the masses of pair-produced semi-invisibly decaying particles at hadron colliders," *JHEP* **04** (2008) 034, arXiv:0802.2879 [hep-ph].

[231] G. Polesello and D. R. Tovey, "Supersymmetric particle mass measurement with the boost-corrected contransverse mass," *JHEP* **03** (2010) 030, arXiv:0910.0174 [hep-ph].

[232] **ATLAS** Collaboration, G. Aad *et al.*, "Performance of the missing transverse momentum triggers for the ATLAS detector during Run-2 data taking," *JHEP* **08** (2020) 080, arXiv:2005.09554 [hep-ex].

[233] **ATLAS** Collaboration, G. Aad *et al.*, "Performance of algorithms that reconstruct missing transverse momentum in $\sqrt{s} = 8$ TeV proton-proton collisions in the ATLAS detector," *Eur. Phys. J. C* **77** no. 4, (2017) 241, arXiv:1609.09324 [hep-ex].

[234] ATLAS Collaboration, "ATLAS data quality operations and performance for 2015–2018 data-taking," *JINST* **15** (2020) P04003, arXiv:1911.04632 [physics.ins-det].

[235] ATLAS Collaboration, "Selection of jets produced in 13 TeV proton–proton collisions with the ATLAS detector." ATLAS-CONF-2015-029, 2015. https://cds.cern.ch/record/2037702.

[236] N. Hartmann, "ahoi." https://gitlab.com/nikoladze/ahoi, 2018.